# General investigations on the heat treatment and thermal fatigue behavior of an experimental hot work tool steel tailored for laser powder bed fusion

Faraz Deirmina[*a1], Lorenzo Quarzago [b1], Daniel Butcher [c], Eleonora Bettini [a], Shahin Mehraban [c], Jonathan Hann [d], Niklas Holländer Pettersson [e], Nicholas Lavery [c], Arne Röttger[*d], and Massimo Pellizzari[*b]

a) Sandvik Additive Manufacturing, Sandvik AB, Sweden
b) Department of Industrial Engineering, University of Trento, Via Sommarive 9, 38123, Trento, Italy
c) Swansea University Bay Campus, Fabian Way, Swansea, United Kingdom SA1 8EN
d) Bergische Universität Wuppertal, Chair of New Manufacturing Technologies, and Materials, Bahnhofstr. 15, 42651 Solingen, Germany
e) Swerim AB, Kista, Sweden

**1. Lorenzo Quarzago and Faraz Deirmina contributed equally and are therefore listed in alphabetical order**

[*] Corresponding authors; Faraz.deirmina@sandvik.com, roettger@uni-wuppertal.de, Massimo.Pellizzari@unitn.it

## Abstract

An experimental hot work tool steel with a leaner chemistry compared to the standard AISI-H13 grade, aimed at enhanced processability, was gas atomized and processed using laser powder bed fusion (L-PBF) to ~99.8% relative density. The lower carbon content (~0.25 wt.% vs. ~0.4 wt.% in H13) resulted in a softer as-built (AB), and quenched martensite (~485 HV1 vs. 625 HV1 in H13), higher martensite-start temperature (~360°C vs. 280-320°C), and about ~18% reduction in dilatation, ascribed to the volume expansive martensitic transformation. Charpy V-notch impact toughness in AB condition (>30 J) was higher than those reported for AB H13. These features account for the improved L-PBF processability. The tempering response in comparison with a wrought H13, was characterized by a larger precipitation of thermally stable Mo- and V-rich secondary hardening alloy carbides at the expense of the easy-to-coarsen Cr-rich ones, attributed to the higher Mo and lower Cr content in experimental alloy. The combination of lower C- and V-contents in experimental alloy, reduced the driving force for the precipitation of coarse vanadium rich carbides during austenitization, as confirmed by electron diffraction spectroscopy (EDS) and synchrotron X ray diffraction. This led to a stronger fine *secondary* hardening alloy carbide precipitation during tempering, and enhanced temper resistance. As elaborated by isochronal tempering, as well as tempering curves, reduction of the elements Si, and Cr shifted the secondary hardness peak to higher tempering temperatures. Consequently, tempering, and thermomechanical softening resistance was significantly enhanced in the new steel with a maximum hardness of ~550 HV1 in over-tempered condition (i.e., slightly above secondary hardness peak). Thermal fatigue (TF) tests revealed a denser and finer TF crack network with a larger oxidation in experimental steel. Thereby, the TF crack penetration depth scaling with the local plastic yielding of the matrix was evidently shorter in the new steel compared with wrought H13, thanks to significantly improved hot hardness, thermal conductivity, and enhanced thermomechanical softening resistance. Finally, a proof of concept is demonstrated by processing a relatively large injection molding die (150 mm × 110 mm × 30 mm) with promising tensile and impact toughness properties after direct double tempering to 51 HRC, and 45 HRC hardness levels.

## 1. Introduction

Laser Powder Bed Fusion (L-PBF) is an additive manufacturing (AM) technology capable of producing components with intricate shapes in a cost-effective way, decreasing both weight and design-to-production times [1–3]. Moreover, L-PBF shows the potential in driving the shift towards a greener production and circular economy. In tooling applications, the design freedom provided by L-PBF has been commercially utilized in the manufacturing of tools, featuring near-surface intricate conformal cooling channels that can otherwise be problematic or not feasible using conventional manufacturing methods (e.g., computer-numerical-control (CNC) milling) [4,5]. This is important in hot forming, or high-pressure die casting, where the main goal is to reduce the cycle times and to improve the quality of the component, as well as productivity thanks to the more uniform and faster cooling [6].

Medium carbon (~0.4 wt.% C) tool steels such as AISI H13, and AISI H11, alloyed with the elements Cr, Mo, and V are widely adopted in hot work applications such as dies for die casting and hot forming applications [7,8]. This class of hot work tool steels has been the most scientifically, and commercially exploited tool steels in laser-based AM processes [9–13]. However, medium carbon hot work tool steels exhibit relatively limited processability through AM, mainly in view of their poor weldability, and residual stress induced cracking, especially when processed without built plate or chamber preheating [9,12,14,15]. The accumulation of thermal and martensitic transformation strains have been reported as the main causes for the gross cracking in extremely hard (600-700 HV) carbon martensite L-PBF processed components, especially in the presence of stress concentrators, and/or if large parts are produced [13,15,16].

It has been demonstrated that optimized scanning strategies and/or built plate preheating (up to 400°C) can help reducing and controlling the thermal strains, thus decreasing the tendency for cracking [9,15,17]. However, martensitic transformation strains cannot be controlled to the same extent, unless preheating with uniform heating efficiency across the build height, and with temperatures above that of martensite start (Ms) temperature (~200-300°C) are employed [9,13]. Hence the need to develop tool steel grades with chemistries tailored for laser-based AM processes. In this regard, alloy development has focused primarily on reducing residual stresses or the ability of the material to accommodate the thermal and transformation strains without cracking. For instance, Röttger et. al. [12] focused on the alloy approach using low transition temperature steels (LTT) employed in welding. Through modified Schaeffler diagrams, and computational thermodynamics, Röttger proposed tool steels characterized by a low Ms temperature. The volume expansion due to martensite transformation caused a reduction in the tensile residual stresses due to the transformation plasticity in the previous austenite phase during fast cooling, while the low temperature transformation suppressed the evolution of high residual stresses as the material shrinks by cooling down to room temperature. Other works report using leaner compositions in terms of element C to reduce the magnitude of the lattice tetragonality and the as-built martensite hardness [18,19], at the same time, decreasing the Ms temperature by increasing drastically the amount of elements such as Mn to ensure that the plate preheating temperature (normally 200°C), is larger than that of Ms during the printing process [18].

In their previous work, the authors focused on the alloy design of a leaner tool steel with improved L-PBF processability, and the ability of the matrix to accommodate the residual stress without the occurrence of cold cracking by introducing a low carbon content modified alloy, [14]. Reduction of carbon (or C equivalent wt.%) plays a key role and imposes a twofold positive effect on reduction of the risk of cold cracking [14,20]

i. Reduction of C reduces the lattice tetragonality (c/a) of the as-built martensite, thus reducing the overall dilatation and transformation strains. This was practiced well before the emergence of L-PBF, in wrought tool steels exhibiting large distortions during quenching, [21].
ii. For the above reason, reduced carbon, decreases the hardness of as-built martensite, increases toughness, and shifts the martensitic transformation to higher temperature, conditions that might favor an easier accommodation of the stresses/strains through a tougher matrix at a higher temperature.

However, in hot working tools, a general requirement is the alloy should achieve a good balance between tempered hardness, toughness, hot hardness, and wear resistance in quenched and tempered condition [8]. Most of these properties are achieved by an optimum combination of carbon and strong carbide-forming elements through tempering of the quenched martensite at temperatures above the secondary hardening peak by precipitation of alloy carbides responsible for the secondary hardening (hereafter secondary carbides) [22,23]. Therefore, any reduction in carbon content, or leaner chemistry should be carefully studied in terms of hardenability, achievable quenched hardness, and over-tempered hardness, wear resistance, and finally mechanical and thermomechanical properties such as thermal fatigue (TF) resistance. In their previous work, the authors introduced an alloy composition, comprising ~ 0.25 wt.% C, with a nominally larger Mo- (~2.0-2.5 vs. 1.5 wt.%), lower Cr- (~2.0-3.0 vs. 5.1 wt.%) and lower V-content (~0.4-0.6 vs. 1.0 wt.%) compared with H13 steel [14]. In this steel, the tempered hardness and the associated properties could be adjusted through increased Mo contents in such a way that there was no loss in the necessary properties despite reduced C and Cr contents [21]. A yield strength of ~1500 MPa, with an elongation at fracture of ~6.5% was achieved by direct double tempering the alloy at 625°C (~490 HV 0.5) from the as-built condition [14], comparable to H13 at similar hardness levels [24]. Moreover, it was shown that the steel possessed an improved printability compared with that of H13 due to its leaner chemistry and lower as-built hardness. However, for the use of the tools employed for hot-working purposes, especially in die casting, the predominant failure mechanism (i.e., > 80% ) revolves around the occurrence of TF cracking, also known as heat checking [7,8,25]. Therefore, a crucial characteristic of hot-work tool steel is its capacity to withstand TF, a property largely determined by fundamental material parameters, including the thermal expansion coefficient, thermal conductivity, hot yield strength, and temper resistance[7,8,25].

In this work, the authors conducted a detailed study on the as built and quenched properties of a novel low C martensitic tool steel, specially developed to be processed by L-PBF. For this steel, the tempering kinetics, tempering resistance, and the thermal fatigue behavior was studied. Thermal fatigue, however, is difficult to be reproduced under laboratory conditions

and, there is no standard test methods in this case. Therefore, to achieve a meaningful comparison, a commercially available AISI H13 grade (wrought) was also tested under similar test conditions.

## 2. Materials and methods

### 2.1. Feedstock powder and L-PBF process

The chemical composition of the gas atomized prototype steel powder used in this research is given in Table 1. The particle size distribution (PSD) reported by the supplier (Sandvik Osprey) is characterized by $d_{10}$, $d_{50}$, and $d_{90}$ of 21 µm, 31 µm and 45 µm, respectively. The elements C, and N were measured by Leco analysis, and the rest of the elements were quantified using inductively coupled plasma optical emission spectrometry (ICP-OES) in compliance with ISO/IEC 17025:2017. The composition range of wrought H13 reference (hereafter H13) is also listed in Table 1.

**Table 1. chemical composition of the alloys, wt.%**

| | C | Si | Mn | Cr | Mo | V | N | Fe |
|---|---|---|---|---|---|---|---|---|
| Prototype | 0.18-0.25 | 0.05-0.30 | 0.10-0.50 | 2.5-3.0 | 2.0-2.5 | 0.35-0.55 | <0.06 | Bal. |
| Powder used | 0.25 | 0.10 | 0.40 | 2.60 | 2.20 | 0.50 | 0.02 | Bal. |
| H13 | 0.32-0.45 | 0.80-1.20 | 0.20-0.50 | 4.70-5.50 | 1.10-1.70 | 0.80-1.20 | - | Bal. |

A Renishaw AM 400 was used to process the samples. After process optimization by processing cubes with dimensions of 15×15×15 $mm^3$, parameters (Exposure Time = 80 µs, Point Distance = 65 µm, Hatch Spacing = 70 µm, and Power = 280 W) yielding a volumetric energy density of ~98.5 $J/mm^3$ were selected. These parameters led to a relative density of >99.8 %, as measured using quantitative image analysis.

### 2.2. Residual stress analysis

Residual stress analysis by X-ray diffraction (XRD) was performed using a Stresstech Xstress G2R X-ray diffractometer in the modified χ method configuration with two symmetrically arranged area detectors. The radiation source was a Cr tube emitting Cr-Kα radiation (0.229107 nm) at a voltage of 30 keV and a current of 9 mA. The collimator had a size of 4 mm. Measurements were performed in three orientations (0°, 45° and 90°) with four tilts in the positive and negative directions per orientation (-45.0°, -37.8°, -30.0°, -20.7, 0°, 20.7°, 30.0°, 37,8°, 45.0°). The exposure time per measurement was 8 s for ferrite/martensite and 30 s for austenite. The residual stresses in the martensite phase were determined from the {211}-reflectance of ferrite/martensite at a 2 θ-angle of 156.40 °, while the residual stresses in austenite were determined from the {220}-reflectance of austenite at a 2 θ-angle of 128.84 °. Measurements were carried out on the last applied layer of vertically built-up cylindrical specimens with a height of 19 mm and a diameter of 7 mm. In addition, a horizontally built-up cylinder with the same dimensions was measured at the last applied layer in the central position. The maximum and minimum principal residual stresses and the FWHM (full width of half maximum) were determined from the measurements. A Young's modulus of 211,000

MPa at a Poisson's ratio of 0.30 for the martensitic phase, and a Young's modulus of 196,000 MPa at a Poisson's ratio of 0.28 for the austenitic phase were considered [12,26]. Cross-correlation with a parabolic threshold of 20% and constant background was used as peak calculation.

### 2.3.Tensile properties and Impact toughness

Tensile tests were performed at room temperature on vertically built cylindrical samples (45 mm in height, and 6 mm in diameter) machined to the dimensions conforming to ASTM E8/E8M-22. Instrumented Charpy V-notch (CVN) tests were carried out according to the ASTM E23-18. For this purpose, samples with dimensions of 55×12×12 $mm^3$ were printed and machined to standard dimensions. The tests were performed on vertically built samples, with the notch plane perpendicular to the building direction. Results were then compared with available results from literature for the L-PBF processed H13.

### 2.4. Tempering kinetics, and tempering curves

The dilatometric specimens (4 mm in diameter; 10 mm in height) were extracted by electro-discharge machining (EDM) from printed cylinders (40 mm in diameter, 20 mm in height). A first set of samples were kept in as-built condition (hereafter AB), while a second one was subjected to austenitization and quenching process (hereafter Q), by heating at 10 K/min to 1020°C, holding for 15 min, and then gas quenching at 100 K/s down to room temperature (RT). Both, AB and Q samples, as well as quenched H13 were then subjected to isochronal heating (10 K/min) up to 700°C to study the possible differences in the tempering behavior. An instrumented quenching and deformation dilatometer (Bähr DIL 805 A/D) was used for all small-scale simulated thermal processes above. Isothermal double tempering (2×2h) treatments were performed in a muffle furnace under protective Ar atmosphere on cubes (15×15×15 $mm^3$) both in AB and Q condition, in the temperature range between 450°C and 650°C. For the Q samples, a prior quenching treatment was performed in a TAV-minijet vacuum furnace at 1020°C for 15 min followed by nitrogen gas cooling (5 mbar) down to room temperature. Hereafter, samples directly tempered from the AB condition are denoted as DT, while the quenched and tempered specimens are referred to QT. Table 2 summarizes the abbreviations used for describing the heat treatment scenarios used in this work. Figs. 1a, and b schematically show the heat treatment schedules with details on the heating rates.

**Table 2. abbreviations used for the samples subjected to different heat treatments**

| Condition | Abbreviation |
|---|---|
| As built | AB |
| Austenitized and quenched | Q |
| Directly tempered from as built condition | DT |
| Austenitized, quenched and tempered | QT |

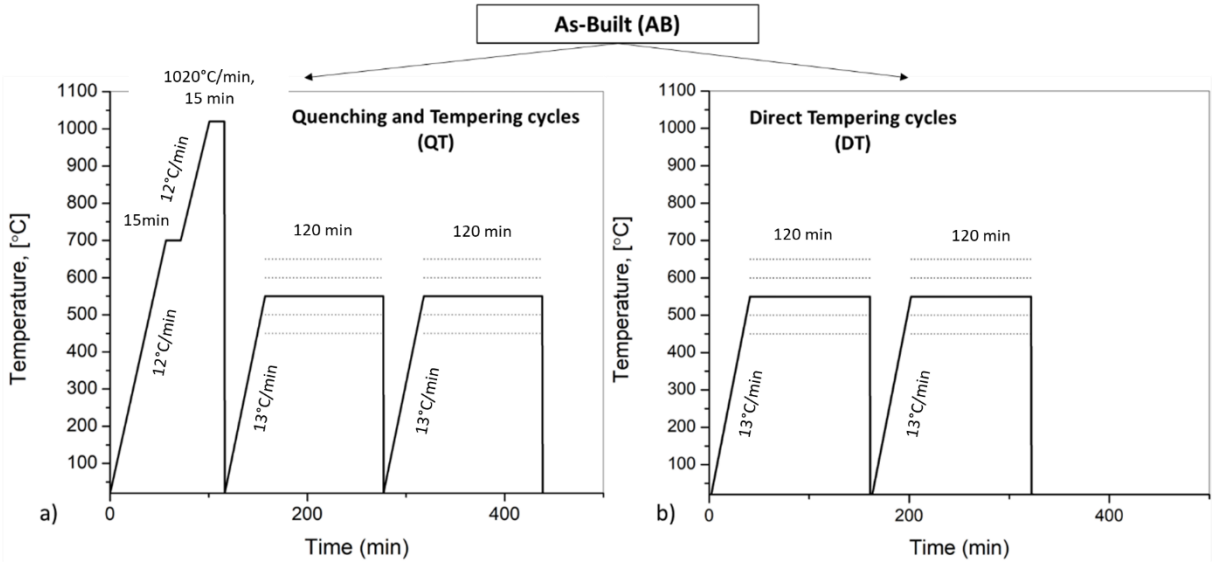


**Figure 1. heat treatment schedules for a) QT specimens, and b) DT specimens**

Moreover, all tempering resistance (temper back) tests comprising hardness measurements after soaking times of up to 40 h, either at 600°C, or 650°C were conducted in the same muffle furnace. Vickers Hardness measurements using a load of 9.81 N (HV1) were performed on the ground (up to 1200 grit), and polished (1 µm finish) cross sections using a (FM310, FUTURE-TECH CORP., Japan) according to ASTM E92-17, with a loading time of 10 s. Rockwell C Hardness measurements were carried out on carefully ground cross-sections (15×15 $mm^2$). The tests were performed in accordance with ASTM E18.

### 2.5.Thermal Fatigue

Thermal fatigue specimens with an external diameter of 42 mm; internal diameter of 16 mm; and a height of 21 mm were fabricated using a plate preheating temperature of 170°C (i.e., standard Renishaw plate preheating system), and were cut from the built plate by EDM without any prior stress relieving (Fig.2a). After the required thermal post processing (i.e., direct tempering, and quench and tempering), samples were turned and ground to reach the final dimensions (a diameter of 40 mm, and height of 20 mm), with a surface roughness (Ra) of 0.4 µm. Tests were conducted using a customary test rig (Fig.2b). The surface of the disk, mounted on a shaft rotating at 4 rpm, was locally heated through an electromagnetic induction system to 630°C ±15C°, constantly read by an optical pyrometer, and successively quenched to 60°C by a water jet with a flow rate of 1.5 $cm^3s^{-1}$. To ensure full homogenization of the temperature on the surface, sample was further immersed in a beaker filled with tap water (~20°C), before starting the successive induction heating cycle. Tests were run up to 1500 thermal cycles, with periodic interruptions for monitoring the TF damage evolution, comprising heat checking density and oxidation on the surface using a light optical microscope (LOM) and ImageJ image analysis software. After completion of the tests (i.e., 1500 cycles), disks were cut, and TF crack depth was evaluated on metallographic cross-sections after grinding and polishing, using ImageJ software on three different cross-sections to improve the statistics of measurements. TF tests were performed on DT and QT prototype alloys, double tempered at 630°C, and 610°C, respectively. For comparison, the commercially

available H13 in QT condition, double tempered at 610°C, was assessed under the same condition.

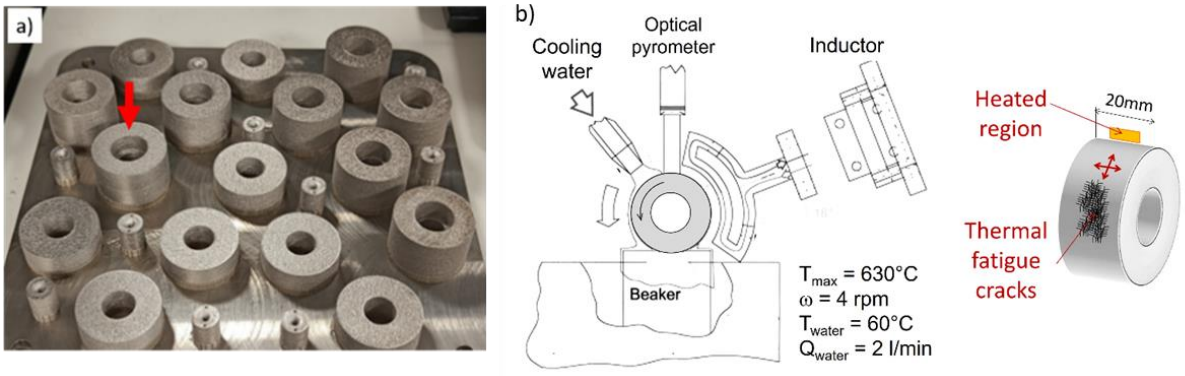


**Figure 2. a) TF disks on the build plate (shown by arrow), and b) test rig and a schematic of TF damage evolution on the disk**

### 2.6. Microscopy and phase analysis

Metallographic cross-sections were prepared by grinding up to 1200 grit, followed by polishing to 1 µm finish, and finally oxide polishing (colloidal silica suspension 0.02 µm). Microstructural characterizations were conducted using LOM, and Field Emission Gun Scanning Electron Microscopy (FE-SEM, Zeiss Sigma, Germany). Electron backscattered diffraction (EBSD) coupled with electron dispersive x-ray spectroscopy (EDS) elemental mapping was conducted using a Symmetry EBSD detector on FE-SEM. SEM imaging and EDS spot analysis was performed using an accelerating voltage of 10 kV (working distance= 8.5 mm), and 20 kV, specimen tilt of 70° and a working distance of 15 mm was used for the EBSD analysis. In EBSD analysis, the magnification was set to 5 kX, and a step size of 0.1 µm was used. Channel 5 suite (Tango mapping) was employed for the post processing of EBSD data. The work of Konijnenberg et. al. [27] was followed for the quantification of the geometrically necessary dislocations (GNDs) density in martensite. Post processing of LOM micrographs for the TF damage was conducted using ImageJ, and Ridge Detection open software.

Thin foils samples for scanning transmission electron microscopy (STEM) were prepared by extraction of 3 mm diameter discs from the QT and DT dilatometry specimens. The dilatometry cylinders were cut into 0.3 mm thick slices and mechanically pre-thinned by grinding using 1200 grit paper down to 0.1 mm thickness prior punching. The punched discs were polished to electron transparency in a twinjet polisher at 30 V in an electrolyte of 10 vol.% perchloric acid in methanol held at -20 ºC. The thin foils were ion polished at 5 kV in a Gatan PIPS system prior the analyses STEM analyses. STEM imaging to detect the nanoscale precipitates was performed using a Jeol JEM-2100F field emission microscope operated at 200 kV.

XRD measurements were performed through an Italstructures (IPD3000) instrument equipped with Cu Kα source (λ=1.5406 Å), in a Bragg-Brentano configuration, from 20° to 120° 2Θ. Data elaboration was performed according to the Rietveld method using MAUD (Materials Analysis Using Diffraction) software [28].

To identify the present phases, particularly the carbides and carbonitrides of $V_8C_7$ and $V_2(C,N)$, diffraction experiments were carried out at the synchrotron radiation source DELTA, beamline 9, at the TU Dortmund. For this purpose, 2D diffractograms were recorded with an incident photon energy of 20 keV (wavelength = 0.61992 Å) and the MAR345 detector. The beam size was height x width = 0.3 x 1.0 mm², and the beam was applied to the sample surface to be measured at an incidence angle of 5°. A diffraction image of a $CeO_2$ reference sample was utilized to calibrate the setup, i.e., detector-sample distance, detector tilt, and beam center, applying the program package Fit2D. The 2D diffractograms were subsequently integrated to obtain corresponding intensity 2Theta diagrams, which were further evaluated using the MAUD software [28], and structural file data from the Crystallography Open Database (COD).

### 2.7. Thermal conductivity

Thermal conductivity calculations were performed on tempered samples, at room temperature and 500°C, by an indirect measurement method, according to the equation 1.

$$\lambda = \alpha C_p \rho \qquad \text{Eq.1}$$

where thermal conductivity $\lambda$, (W/mK), is a product of temperature dependent thermal diffusivity $\alpha$ ($m^2/s$), isobaric specific heat capacity *Cp* (J/kgK), and absolute density $\rho$ ($kg/m^3$).

Laser Flash Analysis was performed on disk-like specimens with a diameter of 12.7 mm; and a thickness of 2 mm, using a Netzsch LFA 467 Hyper-Flash, to determine the thermal diffusivity. Differential scanning calorimetry (DSC) was performed to determine the isobaric specific heat capacity, using the comparison method described in the work of Bernardes et al. [29]. In this regard, thin films with a weight of 50 mg were used. A sapphire reference with known *Cp* was utilized as a reference, and aluminum pans were used to perform the tests. Heating ramps from -10 °C to 40°C were used to measure the *Cp* at the temperature of interest with a heating rate of 20°C/min. The density of the samples was determined at 20°C by Archimedes method following the standard procedure as described in ASTM B311, using a high precision balance on samples with a volume of approximately 1 $cm^3$. The temperature dependent density at 500°C was corrected by using the dilatation records of dilatometry.

### 2.8. Hot Hardness

Hot hardness (HV10) was determined using the Vickers hardness test method based on DIN EN ISO 6507-1:2018-07. Three indentations at room temperature and five at elevated temperature were carried out on the TF disks. For the high-temperature tests, the specimens were first heated to 630°C in an argon environment and held for 20 minutes before the pre-heated diamond indenter was applied with a load of 98.07 N on the metallographically prepared samples surface for 15 seconds. After cooling to room temperature, the indentations were evaluated using a light microscope (Leica DM2700 M), and the hardness was calculated according to the standard. According to the work of Krell et al. [30] measurement error is less than 1% when determining the hot hardness at RT due to the thermally induced volume contraction and can, therefore, be ignored.

### 2.9.Thermodynamic simulations

Thermodynamic calculations of phase quantity diagrams were conducted using Thermo-calc software (TCFE12 database). Thermal conductivity of the alloys was simulated by the property module in Thermo-calc using equilibrium freeze in temperature equal to that of the tempering temperature (i.e., 630°C for DT prototype, and 610°C for QT H13, and QT prototype). Thermal conductivity was simulated for the matrix (BCC) phase. Equilibrium global minimization, and a homogenization function (rule of mixtures, upper Wiener band) was selected. Phase interface scattering constant ($4.0\times10^{-8}$), and 20°C, as the reference temperature for technical coefficient of thermal expansion (CTE) were used following the default values suggested in the software. The thermal conductivity simulations were compared with that of experimental ones, and available literature data. It must be noted that current simulations take the equilibrium condition into account, and therefore must be considered as semi-quantitative results.

## 3. Results and discussion

### 3.1. As built and quenched microstructure, and phases

LOM micrographs in Figs. 3a, and c show an overview of the AB microstructure, the layer-by-layer deposition (Fig.3a), as well as traces of melt pools that are evident in the microstructure after Nital 2% etching (Fig.3c). In higher magnification SEM micrographs (Fig. 3e), the cellular-columnar solidification structure, commonly present in laser-based AM processed alloys, is apparent. Cellular solidification structure is a consequence of constitutional supercooling produced by the fast solidification and is characterized by the heavy micro-segregation effect of alloying elements to the cellular boundaries. It has been demonstrated, and currently well accepted that in additively manufactured tool and maraging steels the intercellular regions can be the preferential zones for retained austenite stabilization (see the inset of Fig. 3e) due to the local enrichment of the alloying elements which generally depress Ms, [31–33]. Indeed, according to XRD analysis (shown in supplementary file 1), a retained austenite volume fraction of about 10 vol.% was present in the AB prototype. This value was lower than reported values in the literature for that of L-PBF processed H13 (i.e., 15-20 vol.% [20,34]) because of the lower carbon and generally leaner chemistry of the prototype alloy [19]. Because of the lower alloy contents, the martensite start and finish temperatures increase, which results in the formation of a lower retained austenite volume content, independent of the segregation effects described above.

LOM micrographs in Figs. 3b, d and f depict the microstructure of the prototype alloy after quenching from 1020°C. It is evident that the layered structure is no longer visible (Fig. 3b), and the melt pool boundaries (weld tracks) are removed because of diffusional reactions, microstructural homogenization, and newly formed austenite grains at high temperature. It is worth mentioning the fine prior austenite grains (PAGs) in the quenched sample. SEM micrograph (Fig. 3f) confirms the removal of cellular solidification structure. The microstructure comprises lath martensite hierarchical structure where inside a PAG (marked by yellow dashed lines) packets of martensite (area confined by red dashed lines) are evident, and inside each packet the martensite block substructure is present (white arrows). XRD

analysis (supplementary file 1) confirmed less than 2 vol.% RA is present in the quenched microstructure because of removal of intercellular microsegregation during the austenitization process. This homogenization of the elements during austenitization causes a global increase in the martensite starting temperature and, therefore, the martensite finishing temperature, which will be shown later using dilatometer tests. Because of the increased Ms and Mf temperatures and the degradation of the microsegregation, the RA content decreases compared to the L-PBF state (higher degree of segregation and locally low Ms temperature).

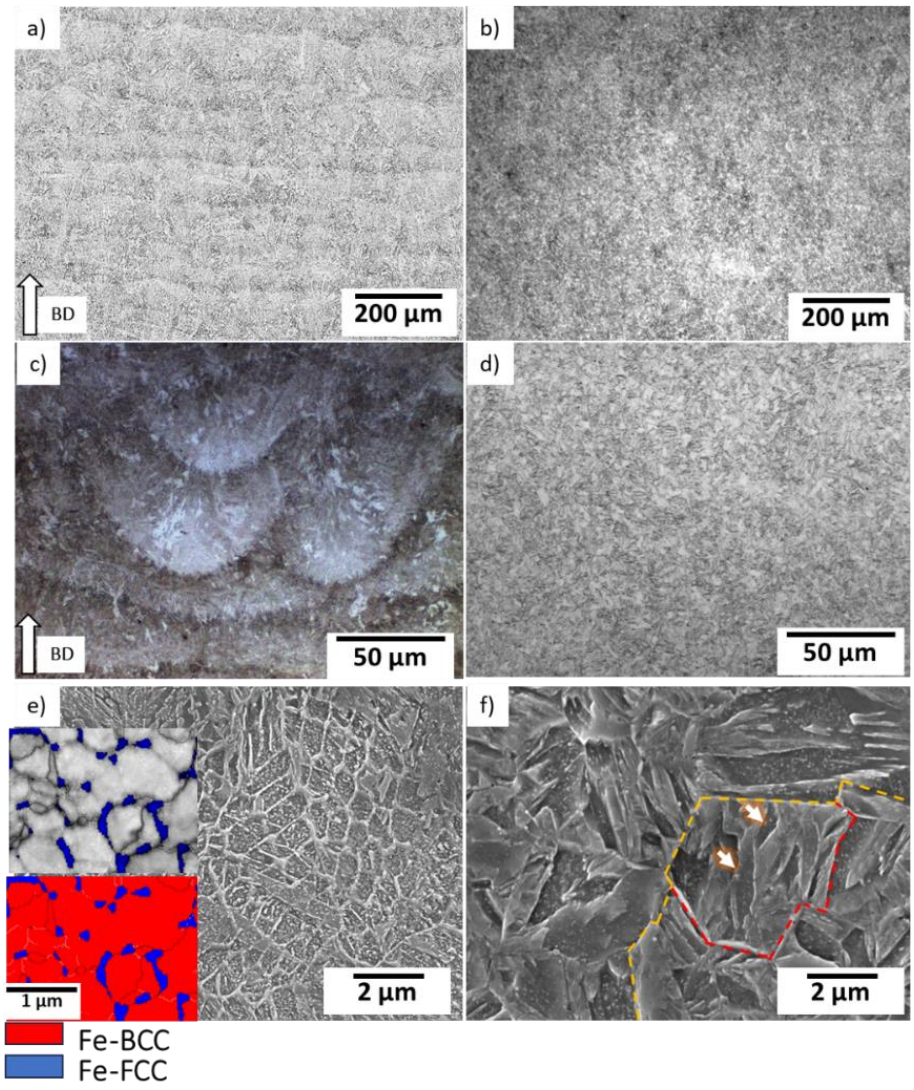


**Figure 3. a, and b) LOM micrographs of as built, and quenched prototype respectively, (100x magnification), c, and d) corresponding 500x magnification micrographs, e, and f) SEM micrographs of as built and quenched prototype respectively, inset in Fig.3e comprise band contrast and phase maps (austenite (FCC) in blue, and Ferrite/martensite (BCC) in red; BD= building direction**

Fine precipitates were present in the as-built microstructure (Fig. 3e). Their presence can be attributed to the intrinsic tempering or aging phenomena caused by the heat transfer from the solidifying layers to the already solidified ones, as evident in C steels, as well as maraging steels [35–37]. However, a feature in the microstructure of the Q material is the presence of fine precipitates within the blocks (Fig. 4a). To the authors best knowledge, this was not

witnessed so intensely in the medium carbon H13 tool steel [34,36,38]. As also shown in Fig. 4b, quenched H13 comprises a fine lath martensite microstructure with the presence of higher vol.% and larger coarse V-rich carbides precipitated during annealing or austenitization process at high temperatures which will be discussed in detail, later in this article.

Indeed, in the lower carbon prototype alloy with a leaner chemistry, the quenched martensite can be divided into 3 distinct regions, i.e.,

i. coarse lath substructures with an evident precipitation of nanosized precipitates
ii. finer lath substructure resembling ridge-like patterns with less evident precipitation, and finally,
iii. regions without precipitates resembling un-tempered quenched martensite.

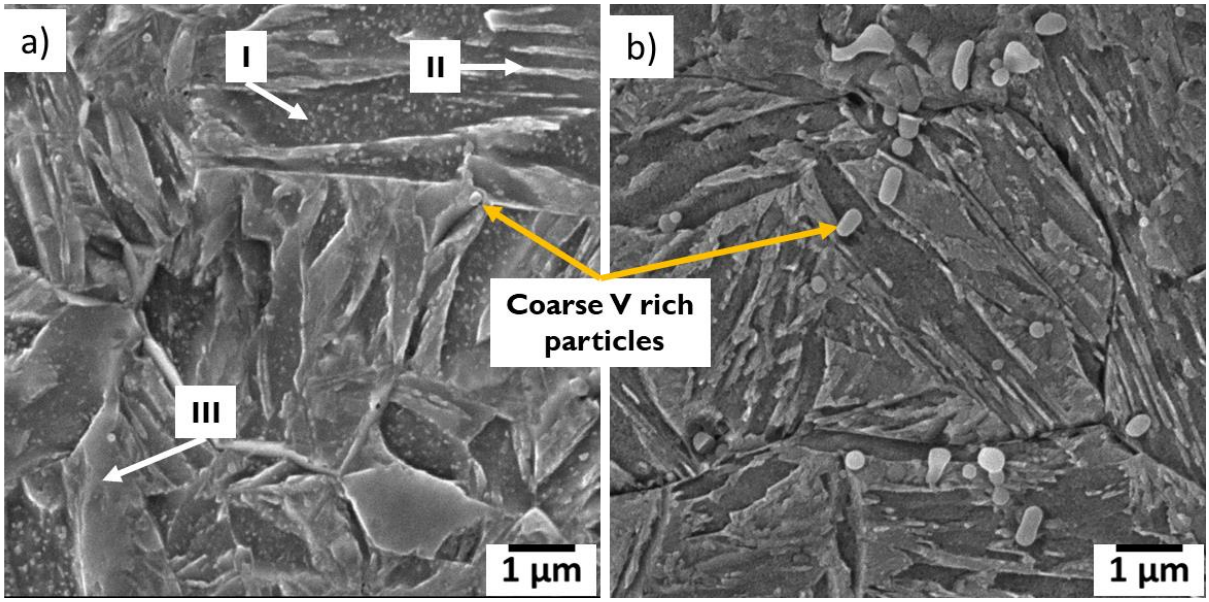


**Figure 4. SEM micrograph of a) Q prototype showing coarse lath substructures with precipitates resembling auto tempering effect (I), finer ridge like lath structure with less evident precipitation (II), and untampered quenched martensite (III), and b) Q H13 comprising untampered fresh martensite and coarse VC particles**

The nano-sized precipitates within the martensite blocks, and at the lath boundaries, (especially the coarser ones) can be ascribed to a partial auto tempering effect in quenched martensite cooled below Ms temperature, by the rearrangement/segregation of the carbon atoms to the dislocations at the lath boundaries [39], and formation of carbides. In particular, precipitation is specific to low alloyed steels with low C contents, and high Ms [40,41]**.** Auto tempering is known to increase the toughness and formability quite significantly [42]. From a laser AM viewpoint, this can be a significant advantage in suppressing cold cracking during the process due to improved toughness, especially if plate preheating is utilized.

## 3.2.Heat treatment behavior

### 3.2.1 Quenching, and martensitic transformation

During heating, the most significant signal of the dilatometric record (Fig. 5a) is represented by the contraction comprised between ~800 °C (i.e., $A_{C1}$) and 890 °C (i.e., $A_{C3}$), corresponding to BCC to FCC transformation. At temperatures lower than $A_{C1}$, multiple

contractions and expansions are recorded and may represent the tempering transformations, which will be discussed shortly. The cooling curve (100 °C/s) showed that the onset of expansion corresponding to Ms temperature was ~360 °C. The cooling curve also represents the completion of martensitic transformation given the record of the expansion peak at about 195 °C (i.e., $M_f$ temperature).

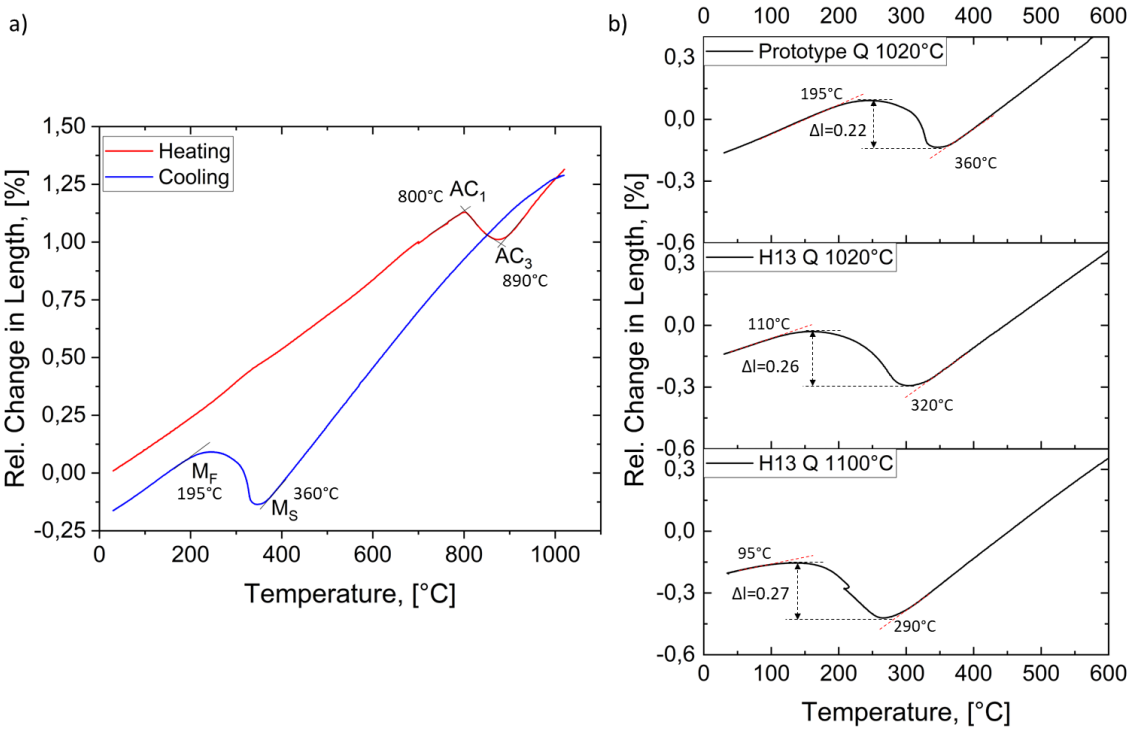


**Figure 5: Dilatometry records of a) austenitization and quenching of AB prototype, and b) volume expansion related to martensitic transformation upon cooling in prototype and H13, quenched from 1020°C, and 1100°C.**

In Fig. 5b, the cooling curve of the prototype alloy is compared with that of an AM H13 using the data from the authors' previous work [43]. If an austenitization temperature of 1020°C (15 min) is considered, the Ms temperature of H13 is lower than that of prototype alloy by 40°C (i.e., Ms~320°C). The dilatation due to the martensite transformation (Δl) in prototype alloy is ~15 % lower than that of H13 (i.e., 0.22 vs. 0.26), meaning that the dimensional changes, distortions, and residual stress build-up due to this transformation can be larger in H13. The reduced dilatation in the prototype alloy is one of the influencing factors in its enhanced L-PBF processability due to the lower residual stress after rapid cooling. This is a consequence of lower C and alloying content in prototype alloy leading to a lower lattice tetragonality (c/a) of martensite compared with that of H13 [41]. However, this is a conservative number. As it is shown by the aid of the equilibrium diagrams (Fig.6a), also reported in Fig. 4b, VC is an equilibrium phase at 1020°C in H13, with a fraction of ~1.1 vol. % in equilibrium state. Therefore, by austenitizing at 1020°C, one should expect the depletion of the matrix from the elements C, and V leading to a quenched martensite with lower C and V content than that of nominal composition. This increases Ms and reduces the dilatation. In rapid solidification process, especially at very high cooling rates of L-PBF ($10^4$-$10^6$ K/s) [10], such diffusional reactions in the solidified material are suppressed, therefore, the dilatation caused by martensitic transformation must be greater because of larger supersaturation of the matrix. For this purpose, cooling curve related to 1100°C austenitization process of H13, where a lower

MC (i.e., VC) volume fraction is stable (i.e., 0.4 vol. %, Fig. 6a) is also shown. The Ms temperature dropped to ~290°C which was 70°C lower than the Ms temperature of the prototype alloy, and dilatation was ~0.27 (~18.5 % larger than that of the prototype alloy) (Fig. 5b). This value represents a more realistic result for the dilatation difference between prototype alloy and that of H13 during the L-PBF process. On the other hand, in the predicted phase quantity diagram of prototype alloy (Fig. 6b), considering 200 ppm N in the starting powder, the vol.% of V(C,N) carbonitrides stable within the austenitization temperature range is still small (i.e., 0.3 vol. %) making a one-to-one comparison with that of H13 quenched from 1100°C more meaningful.

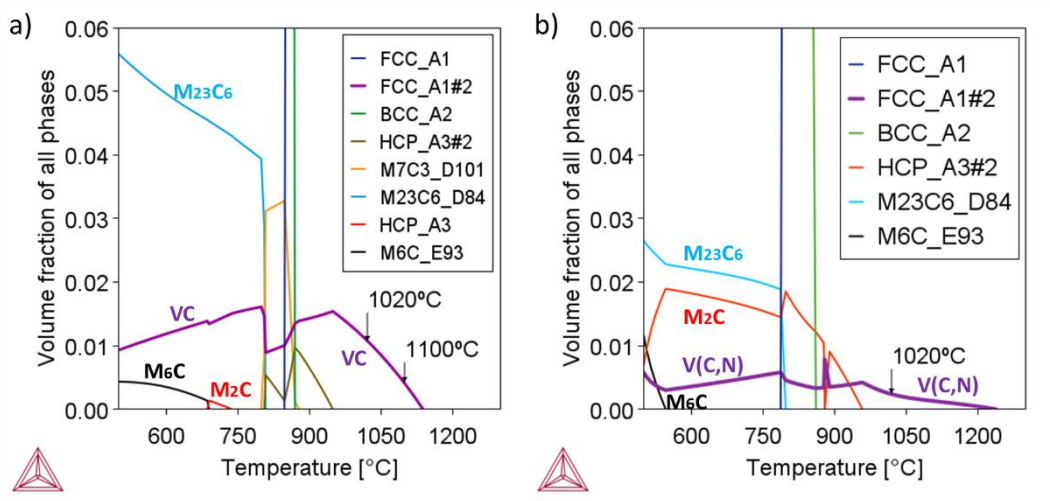


**Figure 6. Phase quantity diagrams of a) H13, and b) prototype alloy composition considering 200 ppm N, HCP phase : $M_2(C,N)$**

The initial hardness of the AB sample (485±15 HV1) is similar to the Q one (486±4 HV1). On the other hand, quenched wrought H13 showed a hardness of 625±5 HV1. This difference in hardness is clearly ascribed to the lower C martensite in prototype alloy. The CVN impact toughness of the prototype alloy in AB was 33.6±0.8 J**.** Impact toughness of the prototype alloy in AB condition was much higher than that of AB H13 (4-8 J) as reported in the work of Kunz et al. [44] and Ackerman et. al. [45], mainly due to the lower hardness of the former and possibly the presence of microcracks and defects in the latter.

Residual stresses in the martensite phase of a conventional H13 processed with L-PBF at a volumetric energy density of 86.8 J/mm$^3$ can be found in the work of Narvan et.al. [46] (Table 3). However residual stress measurements of the austenite phase as a function of measurement orientation are not yet available in the literature. For a similar volumetric energy density, the resulting residual stresses, which are compressive, on the surface of the prototype lie between those of AB H13 (450-690 MPa) and an AB H13 combined with a build platform preheating to 200 °C (100-150 MPa) (Table 3). In the latter the reduction of residual stress was related to the suppression of volume expansive martensitic transformation . It must be noted that in the work of Narvan et. al. [46], almost all non-preheated samples showed gross macrocracks, and according to the authors, this led to an underestimation of the residual stresses due to the reduction of residual stresses because of cracking. The work of Yan et. al [47], on the other hand reports much higher compressive residual stresses (900-1000 MPa) in H13 cubes which were reported to be crack free, however those values seem to be highly unrealistic, as the

tensile strength of RA (normally up to 20 vol.% in AB condition [34]) is considerably lower than 900 MPa and crack initiation from RA become inevitable in case of such high residual stresses [12,48]. It is also noticeable that the residual stresses of RA are shifted towards tensile residual stresses by about 150 - 200 MPa compared to the residual stresses of martensite, similar to the investigations of Röttger et al. [12]. Coupling the dilatometry records of dilatation due to martensitic transformation, softer as-built martensite, with the experimentally measured lower residual stress levels in the as-built prototype compared with AB H13 found in the literature (Table 3), it can be confirmed that for improving the L-PBF processability of hot work tool steels, leaner chemistry can be a solution. It is interesting to note that the martensite finish temperature of the prototype alloy was higher than the plate preheating temperature ( i.e., 195 °C vs. 170°C) reaffirming the hypothesis that plate preheating cannot be effective in suppressing a full martensitic transformation. Therefore, the lower residual stresses recorded for prototype should be attributed to the lower carbon content.

**Table 3. Normal residual stresses at different orientations of the prototype AB as well as of an H13 taken from the literature** *[46]*

| | Prototype AB (vertically built-up cylinder) | Prototype AB (horizontally built-up cylinder) | H13 AB [46] | H13 AB 200 °C preheat [46] |
|---|---|---|---|---|
| Normal residual stress at 0° in RA [MPa] | -118.3±14.9 | -135.0±4.5 | - | - |
| Normal residual stress at 45° in RA [MPa] | -138.0±25.3 | -150.8±16.1 | - | - |
| Normal residual stress at 90° in RA [MPa] | -144.6±25.2 | -174.3±23.5 | - | - |
| Normal residual stress at 0° in martensite [MPa] | -324.5±26.5 | -332.9±2.4 | -688.4±32.9 | -152.9±15.3 |
| Normal residual stress at 45° in martensite [MPa] | -326.9±4.9 | -298.8±4.4 | -556.5±39.9 | -113.2±32.6 |
| Normal residual stress at 90° in martensite [MPa] | -317.4±7.9 | -226.6±12.2 | -450.6±18.6 | -95.6±21.1 |

### 3.2.2 Tempering kinetics

The isochronal heating (10 k/min) behavior to temperatures below $A_{C1}$, was studied to determine the transformations during tempering in AB and Q samples. For comparison, the tempering response of quenched H13 (< 2 vol.% RA) was also evaluated. The first derivative curves of the change in length vs. temperature (dΔ%/dT). In the absence of phase transformations or precipitation/dissolution events (i.e., in fully annealed or over tempered condition) this derivative is given by the CTE. Any deviation from the CTE trend, in the annealed condition, can then be associated with a phase transformation or

precipitation/dissolution event. The subtracted isochronal heating curves in AB, and Q conditions from those of fully annealed ones is represented in Fig.7.

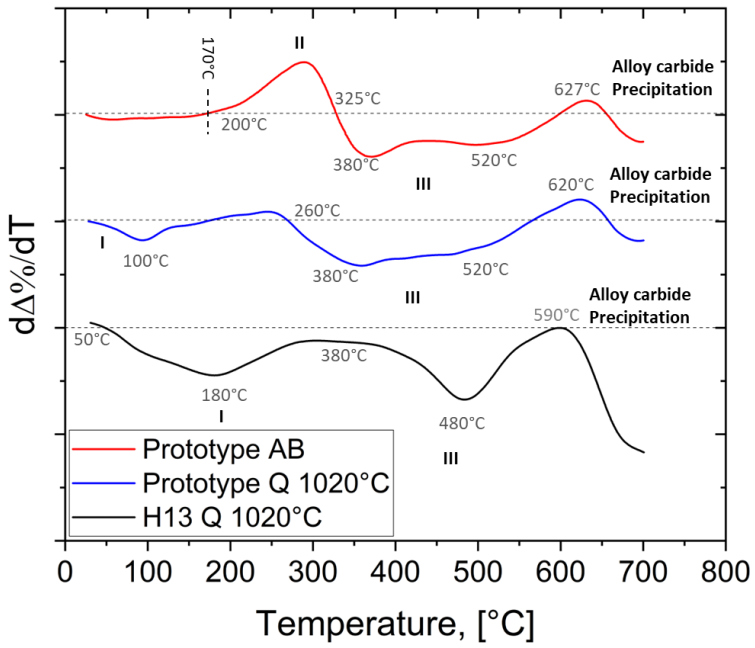


**Figure 7. Dilatation rate during isochronal tempering with a heating rate of 10 K/min for Q H13, and prototype alloys in AB, and Q condition**

Observing the results for the H13, a slight contraction is evident starting from ~50°C, followed by a significantly large contraction showing a peak at ~180°C. According to previous studies, this is ascribed to the transition carbides (ε/η carbide) precipitation (stage 1 of tempering) [49,50]. Stage 1 triggers the loss of martensite tetragonality which is not visible in H13 (0.4 wt.% C) by dilatometry records but quite evident at higher C levels [50]. At a tempering temperature of ~380°C, the onset of a broad contraction with a peak at 480°C is visible. This contraction is due to the cementite (ɵ) precipitation (stage 3 of tempering, ε/η→ ɵ). It is noteworthy to mention that according to a similar research using isochronal heating by dilatometry, and in-situ XRD measurements, the amount of cementite in H13 was negligible, showing a sluggish precipitation behavior in this temperature range [50]. The *classic* stage 2 of tempering is ascribed to RA decomposition in low alloyed steels, however, according to literature, in wrought H13, it appears that highly alloyed RA is stable up to ~500-600°C, and its decomposition starts at higher temperatures [50]. Moreover, due to the insignificant amount of RA in gas quenched H13, this stage will not be evident in dilatometry tests. Finally, at around 590°C, the onset of the largest contraction is visible, which is ascribed to the precipitation of secondary carbides responsible for the secondary hardening of tool steel.

In Q prototype steel (< 2 vol.% RA), a contraction already from RT with a distinct yet low intensity peak at ~100°C is evident. The Q sample was *immediately* subjected to the isochronal tempering after quenching step in the dilatometry, to limit any possible auto-tempering effects. Therefore, the contraction related to the transition carbides precipitation is evident with a lower intensity compared to H13 steel. This is because the contraction associated to transition carbide precipitation becomes less pronounced in low C martensite and is not apparent in martensite containing less than 0.2 wt.% C [51]. Considering the low C

content in the prototype alloy (Table 1), and the partial auto tempering during quenching (high Ms), the precipitation of transition carbides could be mostly suppressed. Further evidence for the easy auto tempering in this steel is given by the presence of intra-block nanosized precipitates in the quenched material stored at RT (see Fig.4b). The dilatometry record shows a quite large and broad contraction, with 2 overlapping peaks, with the onset of 260°C extending to around 525°C, plausibly due to cementite precipitation. The presence of apparently two consecutive peaks should be studied further in detail in future work of the authors. The prototype alloy contains lower elements Si, and Cr (0.1, and 2.0 wt.% respectively) compared with H13 (1.0, and 5.1 wt.% respectively). It is reported that Si, and Cr slow down the cementite precipitation, and growth kinetics [23,52,53]. Even if Si effect is debated by Kozeschnik and Bhadeshiah [54] based on the assumptions that the Si partitioning is not a prerequisite for cementite precipitation in the highly supersaturated martensite, because the driving force for this reaction is large enough even for the para-equilibrium precipitation. However, the same authors claimed that experimental results suggest otherwise, and Miyamoto et. al. [55] showed that para-cementite is difficult to form in the Si-rich martensite (1.0 to 3.0 wt.%) due to the instability of cementite containing Si. Therefore, the authors suggest the anticipated cementite precipitation in the prototype alloy can be a consequence of a lower Si, and Cr content. Finally, a large contraction (still smaller than that of H13) is evident with an onset of 620°C, which is related to the secondary carbide precipitation. It is quite evident that the secondary carbide precipitation in the prototype steel is shifted towards higher temperatures compared with H13 (i.e., 620°C vs. 590°C). This agrees with the anticipated cementite precipitation, and its stability over a wider temperature range in the prototype alloy where the alloy carbide precipitation will be dependent on providing carbon through dissolution/transformation of cementite. The lower intensity of the secondary carbide precipitation peak can be explained by the lower C content of the prototype alloy, leading to lower vol.% of secondary carbides as qualitatively shown in the predicted phase quantity diagrams in Figure 6.

In AB prototype, no evident contraction is seen from RT to around 200°C. In agreement with previous studies [34,43], it seems that the initial tempering process has been completed because of an intrinsic tempering effect during the L-PBF process due to the alternating heat insertion by applying further layer and the use of a plate preheating (170°C, marked by dashed line in Fig. 7). This is in a fair agreement with the microstructural observation (see Fig. 3e). At around 200°C-300°C, a clear expansion in AB is evident. Given the 10 vol.% of RA in AB, this expansion can be related to the RA decomposition to ferrite and cementite (stage 2 of tempering, ($\gamma_{\downarrow\% C} \rightarrow \alpha + \theta$)), the only transformation accompanied by a volume expansion during tempering of steel [49,56]. This is interesting, as the experience from L-PBF H13 suggested otherwise [11,34,57]. In AB L-PBF H13, highly alloyed intercellular RA decomposed to low alloyed austenite and alloy carbides (i.e., $\gamma_{\uparrow\% C} \rightarrow \gamma_{\downarrow\% C} + K$) at temperatures above 500°C accompanied by a contraction in dilatometry record, subsequently the product of this reaction (i.e., $\gamma_{\downarrow\% C}$) transformed to fresh martensite during cooling. This led to a shift to higher temperature in the secondary hardening peak of the directly tempered AB H13 [34,43]. One explanation of the *classic* RA decomposition in prototype alloy, can be the leaner chemistry in view of C, and (Cr+ Mo +V), leading to less stable RA at the

intercellular regions, thus behaving similarly to that of wrought low alloy steels such as AISI 4140 [50]. After this expansion, the overlapping cementite precipitation in AB is evident through the visible contraction (~325°C) in agreement with previous studies [50,56], and finally, the onset of the contraction due to the secondary carbide precipitation at ~627°C is characterized like that of quenched counterpart. The interpretation of the tempering sequence in the prototype alloy proposed here is based on the experimental data collected, and, to the authors experience, it is very plausible. Nevertheless, a complete and correct interpretation would rely on a more extended investigation including techniques, such as transmission electron microscopy (TEM) over the isochronal tempering range.

### 3.2.3. Tempering resistance

The tempering diagram of H13 (Fig.8), shows a secondary hardness peak at ~500°C, at a hardness level of 630 HV,1 which is in agreement with the literature [21]. After this hardness peak, the hardness drops in the direction of a higher tempering temperature due to the over tempering caused by carbides coarsening and increased annihilation effects. In case of prototype alloy, in both DT and QT conditions, the secondary hardness peak is delayed by 75°C compared with H13 (i.e., 575°C vs. 500°C). This agrees with isochronal tempering dilatometric tests (Fig.7), showing a delayed alloy carbide precipitation in prototype alloy. The secondary hardness peaks of QT and DT were ~510 HV1 and ~550 HV1, respectively. At higher tempering temperature, and despite its lower C and alloying content, the prototype alloy in both QT and DT conditions was characterized by a higher tempering hardness than H13, i.e., by higher tempering resistance.

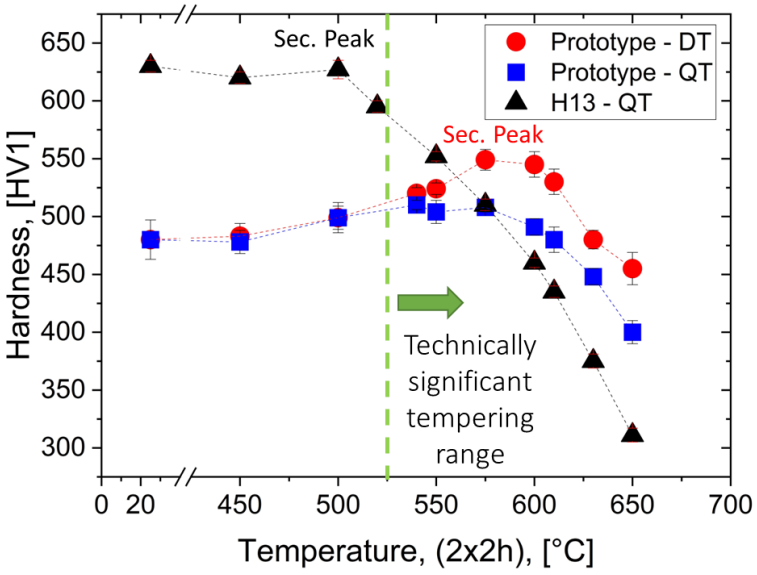


**Figure 8. Tempering curves of prototypes and H13**

This can be ascribed firstly to the secondary hardening peak shift in prototype and secondly to the larger number density ($n_p = \frac{vol.particles}{r_{particle}}$) of the secondary carbides in prototype alloy, where $r_p$ is the radius of the carbides. The latter can be discussed in view of the increased volume fraction of more thermally stable secondary Mo rich carbides compared to that of easier to coarsen Cr rich secondary $M_7C_3$ and $M_{23}C_6$ ones. Therefore, by reducing particle

radius, the number density increases, leading to the increased strengthening effect according to Orowan strengthening mechanism. This was a consequence of higher Mo and lower Cr content in the prototype alloy (see Fig.6) [14]. Indeed, Sonderegger et al. [58], showed experimentally that the radius of secondary Mo-rich ($M_2C$) and V-rich (MC) carbides were around 1.5 nm in steel H11 tempered at 600°C, while at the same condition, Cr rich ($M_7C_3$, and that of equilibrium $M_{23}C_6$) secondary carbides were ~8.0 nm in size. The over-tempering at higher temperatures and longer times (i.e., 650°C, 24 h) led to the growth of $M_2C$ to 11 nm before transforming to $M_6C$ ones, and thermally stable MC type carbides coarsened to ~11 nm, while Cr-rich carbides size increased to ~55 nm. This was backed by the thermodynamic modeling in the same work, as well as the work of Eser et al. [59] .

At similar tempering temperatures, especially from the secondary hardening peak onwards, a relatively constant difference of ~ 30-40 HV1 is witnessed for the DT and QT prototype tool steel. The higher hardness of DT, can be ascribed to the larger *initial* dislocation density characteristic of rapid and far from equilibrium solidification, promoting increased nucleation sites and thus considerably finer secondary carbide precipitates [20,43]. However, the main reason for this behavior is most likely the slightly larger elements C and V in solid solution of the AB samples, leading to larger precipitation of the most thermally stable and extremely fine *secondary* V(C,N). As it was shown in the quantity phase diagrams (Fig. 6b), the presence of N, enhanced high temperature stability of V(C,N) at 1020°C (austenitization temperature). At this temperature, a maximum of 0.2 vol% of V(C,N) could be precipitated during austenitization process of the prototype alloy. Therefore, in quenched prototype, one expects slightly less available C, and V in quenched martensite, for the later precipitation of extremely fine *secondary V(C,N)* during the tempering process. This leads to a slight drop in temper resistance of the quenched and tempered steel. This effect was clearly shown in the work of Sjöström and Bergström [8] on a wrought H13 tool steel, whereby increasing the austenitization temperature close to the dissolution temperature of equilibrium VC, thus providing larger vol.% of secondary VC during tempering, the tempering resistance was significantly increased. This will be shortly discussed in section 3.3 by microstructural characterization of the tempered martensite.

From an industrial viewpoint, H13 is normally used in over tempered condition (i.e., technically significant tempering range shown in Fig. 8) due to its typical service temperatures (~400°C to700°C) which necessitates high thermal stability (i.e., tempering resistance) by over-tempering. Moreover, toughness improves by over tempering above the secondary hardness peak [21,57]. Looking at the current results, it is suggested that prototype alloy, tailored for L-PBF process, can recover the required tempered hardness in the over tempered condition.

Tempering resistance tests were performed at 600°C, and 650°C, up to 40 h on H13 (*2x2h, 610°C- 440±3 HV1, see Fig. 8*), QT-prototype (*2x2h, 610°C-475±5HV1, see Fig. 8*), and DT (*2x2h, 630°C-480±8 HV1, see Fig.8*). These specimens were later used for microstructural analysis and thermal fatigue. The results are depicted as a function of Larson-Miller tempering parameter (Tp), where Tp can be calculated by $TP=(273.15+T)\times(\log(t)+20)/1000$,

whereby T is the tempering temperature in degrees Celsius, and t is the tempering time, in hours (Fig. 9).

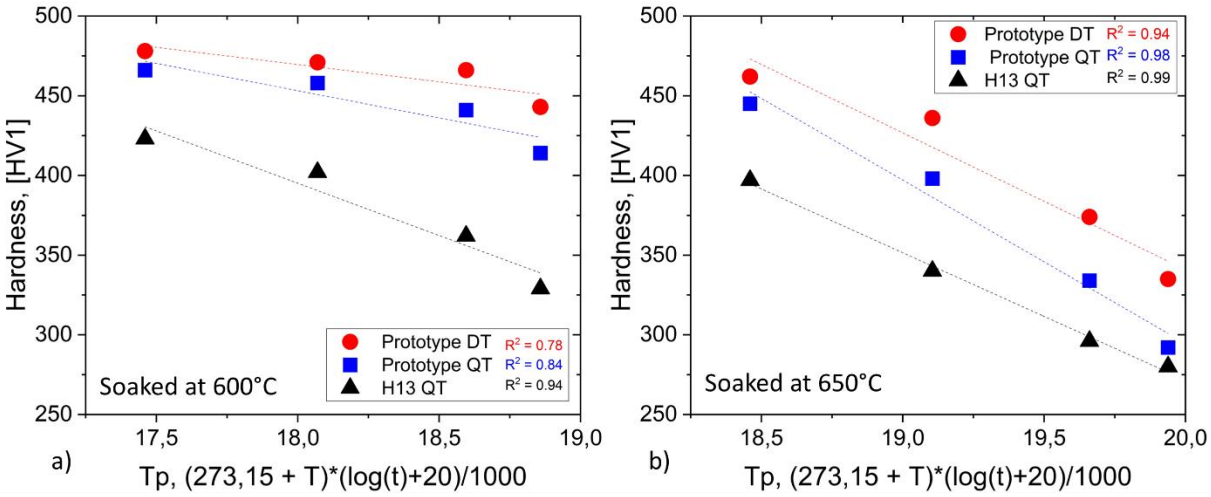


**Figure 9. Hardness vs. Larson Miller tempering parameter at a) 600°C, and b) 650°C**

At 600°C (Fig. 9a), the hardness of H13 dropped by ~100 HV1 after 40 h of soaking. In the case of the prototype alloy, the drop was ~50 HV1, while steel in DT condition showed slightly higher hardness than in QT condition. Given the similar initial tempering temperatures of QT H13, and QT prototype (i.e., 610ºC), the tempering resistance of the prototype alloy was higher than H13. Over tempering at 650°C (Fig. 9b), led to stronger softening in all alloys because of accelerated Ostwald ripening of the secondary carbide, justified by the relatively lower thermal stability of samples tempered at lower temperatures (i.e., 610, and 630ºC), compared with that of the test temperature (650ºC). In the case of the steel H13, hardness was dropped by 160 HV1 to ~280 HV1 after 40 h. In contrast, in the prototype tool steel, DT was characterized by a drop in hardness of ~150 HV1, and QT showed the largest softening rate, where hardness dropped by 180 HV to ~290 HV1 after 40 h. The results suggest that the tempering resistance of the prototype steel is at least equal to that of steel H13 in quenched and tempered state, while, in case of direct tempering, with the initially higher tempering temperature, and larger supersaturation of the matrix in V, and C, the tempering resistance is higher.

### 3.3. Tempered Microstructures

The EBSD coupled with EDS mapping results for the wrought H13-QT-440 HV1, and the prototype alloys (i.e., DT-480 HV1, and QT-475 HV1) is shown in Fig. 10. In band constrast (BC) maps, boundaries with misorientation angles larger than 15° (high angle boundaries) are shown in blue, and those larger than 2° are in red (Figs.10a-c). The parallel crystal alignment representing the blocks of the lath martensite is evident in all alloys, as also confirmed by inverse pole figure maps (IPF-X) in Figs. 10 d-f. Block width measured by line intercept method using misorientation angles >10° [60,61] on the EBSD maps (Table 4 ), confirmed the finer block size in H13 (i.e.,500 nm) compared with those of prototype tool steel (660, and 600 nm for DT, and QT respectively). According to Morito [60], block width in lath martensite scales with the C content, and larger C in H13 led to a finer block size.

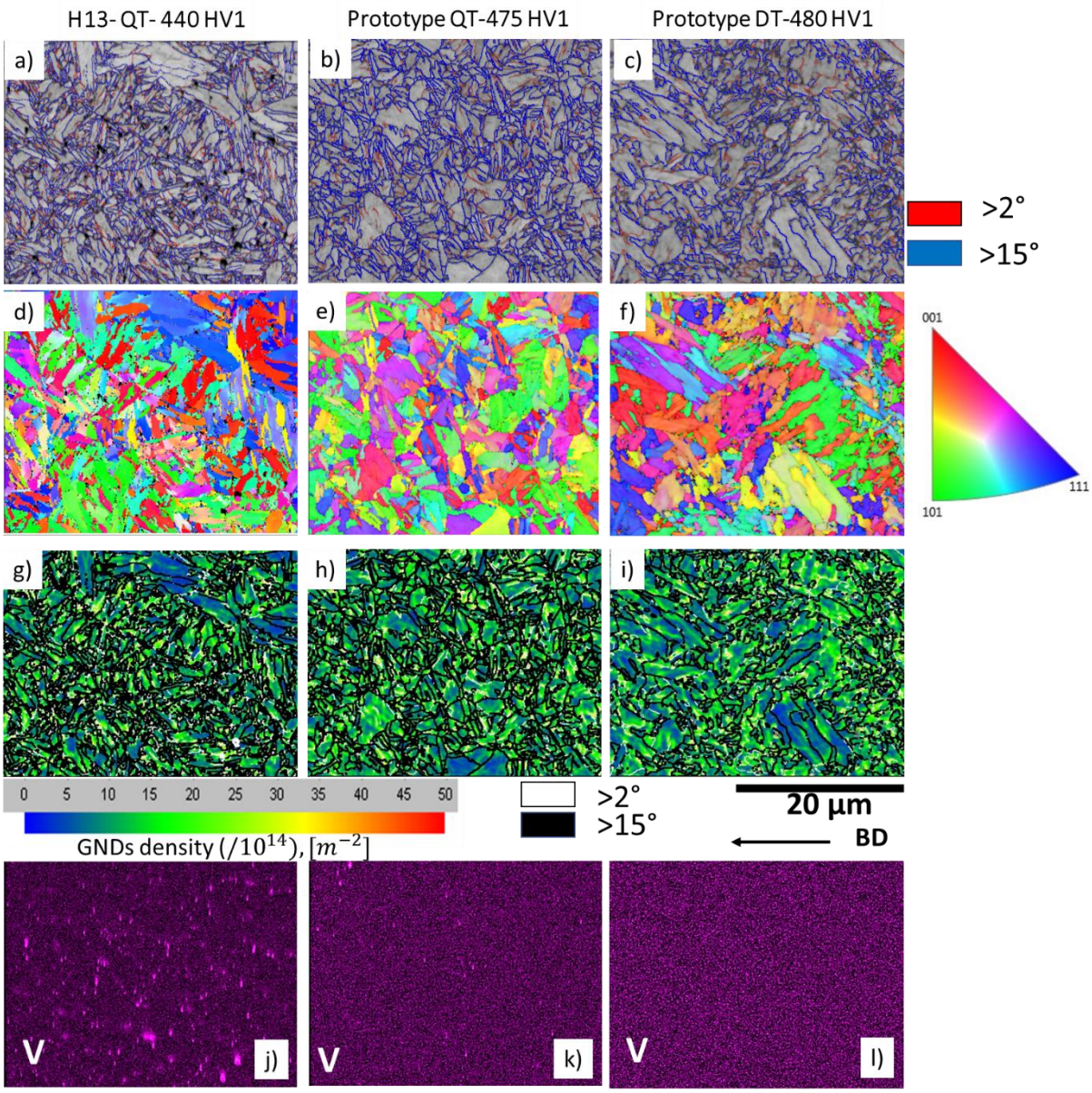


**Figure 10. EBSD and EDS mapping results of QT H13 (2×2h at 610°C, 440HV1), QT prototype (2×2h at 610°C, 475 HV1), and DT prototype (2×2h at 630°C, 480 HV1): a-c) BC maps overlaid by boundaries with misoreintation angles of >2˚(red), and >15˚(blue), d-f) corresponding IPF-X maps, g-i) corresponding GNDs density maps , note in GNDs density mapping boundaries with misoreintation angles >2° are in white and that of >15° in black for a better contrast and j-l) corresponding EDS maps for vanadium**

The geometrically necessary dislocations (GNDs) maps (Figs.10g-i) show that the dislocation density is larger within the blocks and plausibly at the lath boundaries. This is not susprising as it is well accepted that in lath martensite, laths within blocks form to minimize the strain energy resultants of the lattice distortions around carbon atoms during martensite transformation. The lattice strain is accommodated by the interfacial dislocation generation at the lath boundaries (i.e., low angle boundaries in martensite hierarchy) [39]. The GNDs density (Table 4) peaked at ~$1.4\times10^{15}$ $m^{-2}$ for H13 and QT prototype, while it was lower in DT sample (i.e., ~$1.3\times10^{15}$ $m^{-2}$). This agrees with the higher tempering temperature of DT sample, 20°C higher than those of QT prototype and H13 (i.e., 630°C vs. 610°C). The dislocation density is known to drop rapidly in the very early hours of tempering, and the final

dislocation density decreases by increasing the tempering temperature. Therefore, even if the AB condition must have the largest dislocation density due to rapid solidification, the tempering process at temperatures higher than that of the dislocation recovery, causes a significant drop in dislocation density within a very short time [20]. The numbers are in the range of those reported for H13 (tempered at 640°C) measured by XRD, and an order of magnitude lower than that of quenched martensite in H13[62].

**Table 4. block width and GNDs density results for QT H13 (2×2h at 610°C, 440 HV1), QT prototype (2×2h at 610°C, 475 HV1), and DT prototype (2×2h at 630°C, 480 HV1)**

| | EBSD - Magnification | Step size [μm] | Mean Block width [μm] | Standard deviation | Variance | Size of dataset | GNDs denisty ($/10^{15}$) [$m^{-2}$] |
|---|---|---|---|---|---|---|---|
| H13 QT | 5kX | 0.1 | 0.50 | 0.38 | 0.61 | 10300 | 1.36 |
| Prototype QT | 5kX | 0.1 | 0.60 | 0.62 | 0.39 | 8855 | 1.39 |
| Prototype DT | 5kX | 0.1 | 0.66 | 0.75 | 0.56 | 8024 | 1.28 |

EDS mapping for V, confirmed the large presence of coarse V rich carbides (0.78 vol.% according to image analysis) resultant from either *annealing or austenitization process* in H13 (Fig. 10j). In comparison, the size and vol.% (0.15 vol.%) of V rich particles in QT protopye is smaller than that in the microstructure of steel H13 (Fig. 10k) in agreement with discussions in Fig. 6. On the other hand, DT prototype steel, without any prior austenitization, does not exhibit the precipitation of large carbides (carbonitrides), as V mapping did not reveal any locally large V concentration (Fig. 10l). From the SEM micrographs, and looking at the EDS spot analysis results, it was, at least semi-quantitatively, further confirmed that large vanadium rich carbides precipitated during *annealing and austenitization* exist in H13 (Fig. 11a). A smaller size and vol.% of vanadium rich carbonitrides are observed in QT prototype tool steel (Fig. 11b) in agreement with the phase quantity diagrams in Fig.6, and EBDS results in Fig. 10. DT microstructure does not contain large V rich carbides (Fig. 11c) as a result of avoiding high temperature austenitization. To further confirm the type and structure of these carbides, synchrotron diffraction results on quenched samples is presented in Fig. 11d. The secondary hard phases are vanadium-rich carbides or carbonitrides with a face-centered cubic structure (space group Fm-3m). It is generally known from the literature that, contrary to stoichiometric VC carbides, substoichiometric carbides of $V_8C_7$ or $V_6C_5$ form [63]. Substoichiometric vanadium carbides of type $V_8C_7$ were determined for the H13 steel sample. Considering the wavelength and the respective 2Theta angles, the lattice parameter was determined to be a= 0.4164 nm (hkl=111). In the literature, a lattice parameter of 0.4164 nm (V/C ratio = 0.872) to 0.41645 nm (C/V ratio = 0.876) is mentioned for the $V_8C_7$ phase, depending on the V/C ratio. In this work, a gas-atomized powder was used, and nitrogen was used as an atomization gas. Nitrogen has a certain solubility in steels and, like the element carbon, forms stable nitride compounds with the transition metals of the 4-6 subgroup. If nitrogen and carbon are present at the same time, carbonitrides can form. Considering the work of Chen and Jiang [64] vanadium carbonitrides ($\Delta Hf$= -0.707 eV/atom for $V_2CN$) have a lower standard enthalpy of formation and are therefore thermodynamically more stable than the phases vanadium carbide ($\Delta Hf$= -0216—0.33 eV/atom for VC). The lattice parameter of vanadium carbonitrides lies between the lattice parameters of $V_8C_7$ (a= 0.4164 nm) and VN (a= 0.4126 (N/V=1)) [65]. Our measurements confirm that the lattice parameter for phase $V_8C_7$ in the sample H13-QT with a = 0.41106 nm is slightly larger than for the lattice parameter in the prototype alloy, a = 0.41022 nm. For this reason, it is assumed that the powder absorbed a certain nitrogen content during the gas atomization process (see table 1,

and EDS analysis in Fig 11b), so that stable vanadium carbonitrides instead of vanadium carbides are formed in the prototype alloy.

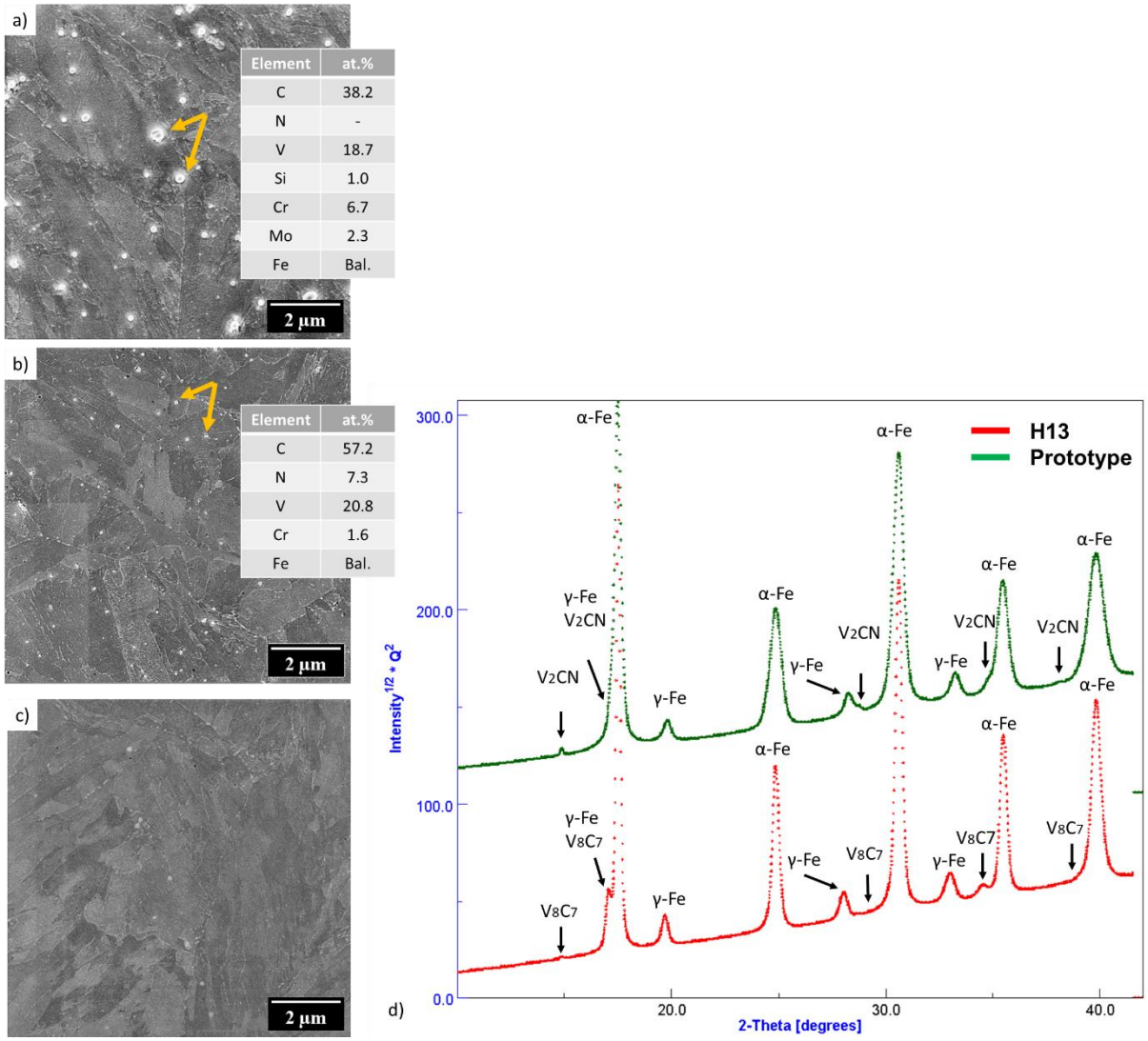


**Figure 11. a-c) in-lens SEM micrographs of QT H13 (2×2h at 610°C, 440 HV1), QT prototype (2×2h at 610°C, 475 HV1) , and DT prototype (2×2h at 630°C, 480 HV1) respectively, EDS spot analysis results in at.% is added for coarse V rich carbides (carbonitrides) precipitated during high temperature austenitization, and d) Synchrotron diffraction results for H13 and Prototype in quenched condition elaborating on coarse V rich carbides (carbonitrides)**

In all tempered conditions, the precipitation of *fine secondary* carbides, especially at the lath and block boundaries, is evident (marked by arrows), and it is possible to postulate that the size of the secondary carbides is largest in H13 steel in wrought and heat-treated condition, while prototype in DT condition exhibits a finer carbides size compared with that of QT prototype (Figs. 12a-c). The latter is shown more clearly in STEM results in Figs.12 d and e, where the *secondary* carbides (arrows) number density is larger in DT (Fig. 12e) compared with QT ( Fig.12d), and the carbide size is clearly finer in the former. The EDS analysis on the precipitates, shown in supplementary file 2, highlights V, Mo, and slight Cr enrichment that can be characterized as MC, and plausibly $M_2C$ [58]. Moreover, in agreement with the alloy design philosophy in reducing Cr, no indications of $M_{23}C_6$ or $M_7C_3$ Cr rich carbides was identified in STEM analysis. Carbides morphology agree well with the literature results on

tempered H11, and H13 tool steels [58]. The results highlight the considerable benefit in avoiding austenitization and quenching prior to tempering in view of suppressing large carbides (carbonitrides) precipitation thus maintaining a highly supersaturated martensite, as well as benefiting from the high dislocation density in AB condition which results in a finer distribution of secondary carbides upon tempering.

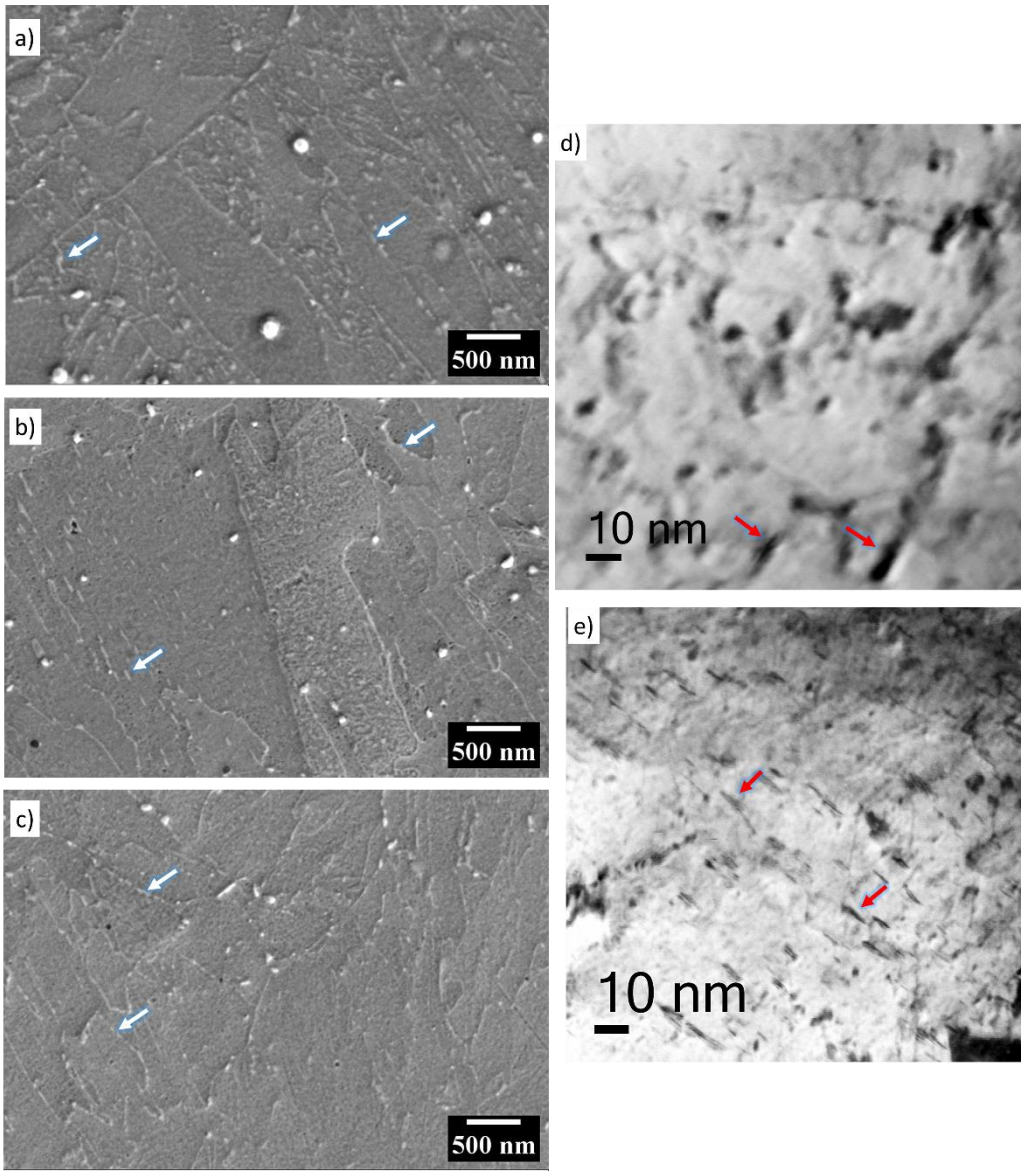


**Figure 12. a-c) FEG-SEM micrographs of QT H13 (2×2h at 610°C, 440 HV1), QT prototype (2×2h at 610°C, 475 HV1) , and DT prototype (2×2h at 630°C, 480 HV1) respectively, d) STEM images of QT prototype, and e) STEM images of QT prototype**

To summarize, despite a lower hardness (440 HV1), H13 had the finest block width compared to QT (475 HV1) and DT (480 HV1) prototypes. Moreover, the dislocation density in H13 was at least larger than that of DT because of a lower temperature tempering. It is well known that in tempered martensite, strengthening can be ascribed to i) Hall-Petch, considering the width of the blocks as the smallest constituent of lath martensite characterized by high angle boundaries [61,66,67], ii) dislocation and iii) particle (secondary carbides) strengthening, the last contributor is solid solution strengthening which plays a minor role in tempered martensite strength [61,66,68]. In view of the larger Hall-Petch contribution in H13 (finer

block width), as well as its larger dislocation density compared with the DT, and like that of QT prototype, now it is more convenient to postulate that the hardness difference in the prototype alloys compared with that of H13 stems from their improved particle strengthening contribution due to finer size, in *over tempered* condition as discussed in the tempering resistance section of this manuscript and experimentally shown by the SEM and STEM analysis. With regards to enhanced temper resistance of DT prototype over that of QT, microstructure and synchroton results confirmed the previous observations in section 3.3, where the larger martensite supersaturation in elements V, and C, achieved by avoiding large V rich carbides (carbonitrides) precipitation during the austenitization, can be responsible for the precipitation of a larger vol.% and finer *secondary* Mo and V rich carbides during tempering. V rich MC particles formed during tempering are known as the main contributors to strengthening at eleveated temperatures (i.e., >600°C) due to their extremely fine size, and resistance to coarsening [20,43,58,59]. Presence of element N in prototype alloy leads to the precipitation of more thermally stable secondary V rich carbonitrides compared with that of secondary MC ones [43].

### 3.4. Thermal conductivity in tempered condition

According to the thermal conductivity measurements at RT, QT H13, QT and DT prototype tool steel showed values of 23.3, 35.0 and 34.8 W/mK, respectively. At a testing temperature of 500°C, these values were 27.0, 32, and 33 W/mK, respectivetively (Fig. 13). In order to predict for a wider temperature interval, thermodynamic calculations using Thermo-Calc software were carried out for H13, H10, and prototype steel with a freeze in temperature of 610°C for QT and 630°C for DT-prototype (i.e., to mimick the equilibrium at the tempering temperatures). For comparison purposes, the experimental thermal conductivity data for H13 and H10 steel in tempered condition (430-450 HV30) is plotted [69]. With regard to wrought H13 tempered to 430-450 HV30, the simulated trend agrees quite well with the experimental data up to 500°C [69]. The calculated curves tend to deviate from experimental data starting from 500°C, and become siginficantly divergent at 600°C. The thermal conductivity increases with increasing tempering temperature, which is attributed to the increased precipitation of carbides so that the phononic component is greatly increased [70]. Ultimately, the thermal conductivity increases with increasing carbide formation and the associated setting of elements. These elements set in carbides no longer distort the lattice, which increases thermal conductivity [70]. This could not be captured by the equilibrium freeze in temperature settings in Thermo-calc as the experimental measurements are carried out on non-equilibrium microstructures. For H10 steel that needs a higher tempering temperature than H13 to achieve a tempered hardness of 43-45 HV30, the simulated curves seem to better fit experimental data in the whole temperature range where the original tempering temperature should have been higher than 600°C leading to the stabilization of microstructure up to 600°C [69]. The

simulated curves for prototype alloys showed a slight overstimation compared with experimental values probably due to the residual porosity in L-PBF samples [71].

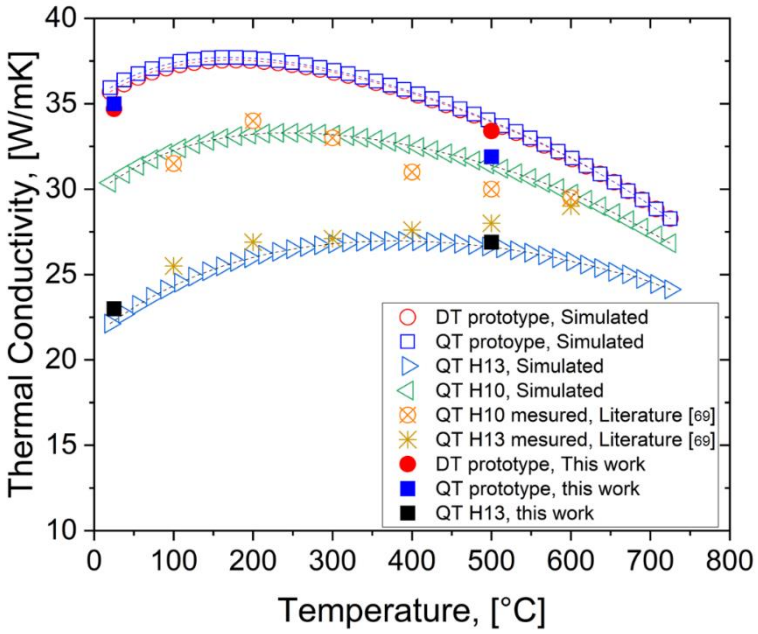


**Figure 13. Measured, and simulated thermal conductivity for QT H13 (2×2h at 610°C, 440 HV1), QT prototype (2×2h at 610°C, 475 HV1), and DT prototype (2×2h at 630°C, 480 HV1), results from literature [69], are included in this graph**

Given the general agreement between the simulated curves and those experimentally measured, it is plausible that the lower amount of elements Si, and C in prototype alloy corresponds to improved thermal conductivity compared with H13 over a wide temperature range [70]. Indeed H10, with a nominal Si, and C content of ~ 0.3 wt.%, lies in between of prototype alloys (0.1 wt.% Si, 0.25 wt.% C), and that of H13 (0.95 wt.% Si, 0.4 wt.% C).

## 3.4. Thermal Fatigue damage

### 3.4.1. Surface TF cracking, and oxidation

The surface TF damage evolution of different samples is reported in Figure 14. Promptly after 500 cycles, thermal fatigue cracking networks (heat checks) appeared on the surface of all the specimens (Figs. 14a-c), similar to the typical damage found in many tools and dies. Cracks were uniformly distributed on the surface, and in the initial stages of TF damage, it was possible to observe that pores in the L-PBF prototype steel served as the preferential crack initiation sites (shown by arrows). After 500 cycles, cracking in H13 occurred preferentially normal to the revolution direction (RD), where the applied thermal stress is higher, while prototype steel samples already show a more uniform bidirectional cracking with the emergence of TF cracks along the transversal direction (TD, i.e., along RD). Nucleation of the thermal cracks is results from the local plastic yield of the tool material on the surface after cyclic heating and cooling. Indeed, in brass die-casting experiments, 500 die casting cycles were enough to observe the nucleation and propagation of the initial thermal fatigue cracks on the surface and into the core [25]. Consequently, the temperature gradients on the tool surface, during heating and cooling are severe enough to impose compressive stresses, leading to the

local accumulation of plastic strains to nucleate and propagate thermal cracks through a low-cycle fatigue process [7,25]. By increasing the number of cycles, heat checking damage gradually increased in terms of crack length and interconnection (Figs. 14d-f). In H13, bidirectional cracking became evident after 750 cycles (Fig. 14d) with the emergence of leading cracks (thicker, and longer ones shown by arrows), while less evident long and thicker cracks was found for the prototypes (Figs. 14e, and f). The oxidation attack on the surface, and crack network filling by oxides, became more severe by continuation of the cycles, a higher magnification image of oxidation attack will be presented later in this paper. A significant difference between H13 and prototype steel, might be associated to the evolution of a finer, yet denser crack network in the latter irrespective to the heat treatment schedule (Figs. 14e, and f). After 1500 cycles, the crack length further increased normal to the RD, and an interconnected network of heat checking damage was evolved for all the samples (Figs.14g-i).

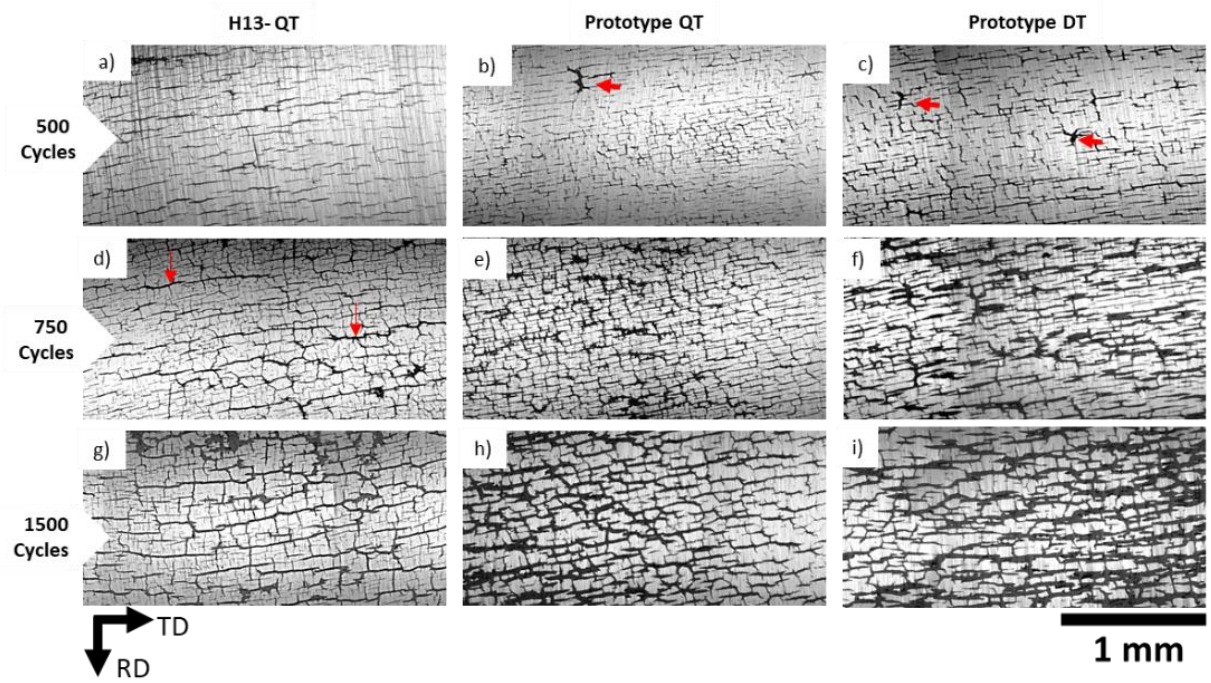


**Figure 14. Surface condition of QT H13 (2×2h at 610°C, 440 HV1), QT prototype (2×2h at 610°C, 475 HV1), and DT prototype (2×2h at 630°C, 480 HV1), respectively after several TF cycles (630°C↔60°C) : a-c) 500 cycles d-f) 750 cycles, and g-i) 1500 cycles, arrows address possible pores or printing defects served as crack nucleation sites**

A quantitative evaluation of the cumulative cracking density ( i.e., the area fraction of the crack network) indicates a higher cracking rate up to 500 cycles. At 750 cycles onwards, the heat checking rate becomes slower because of the interconnection of the existing cracks, and possibly thermal stress relaxation by the penetration of the leading cracks towards the core (Fig. 15a). This is also shown by the measurement of heat check density growth rate as well (Fig. 15b). The main differences between H13 and prototype steel is the larger surface crack density in the late stages of thermal cycling (i.e., 750 cycles onwards, Fig. 15a), where after the completion of the test the cumulative heat check density was approximately 50% higher in QT and DT prototypes (Fig. 15a). Moreover, QT and DT prototypes clearly showed more severe oxidation damage. This can be a consequence of lower Cr as well as Si in this steel.

Also, as shown in Figure 16, the crack nucleation on the surface during the early stages of test, preferentially occurred at the prior austenite grain boundaries in both QT materials (Figs.16a, and b). A finer PAG size of the prototype (Fig.16b), a consequence of the rapid solidification process and short time austenitization at 1020ºC, increases the grain boundary area and enhances preferential oxidation attack at the high angle grain boundaries. In the case of DT prototype, the oxidation seemed to have been started at the block boundaries (i.e., still high-angle boundaries) (Fig.16c).

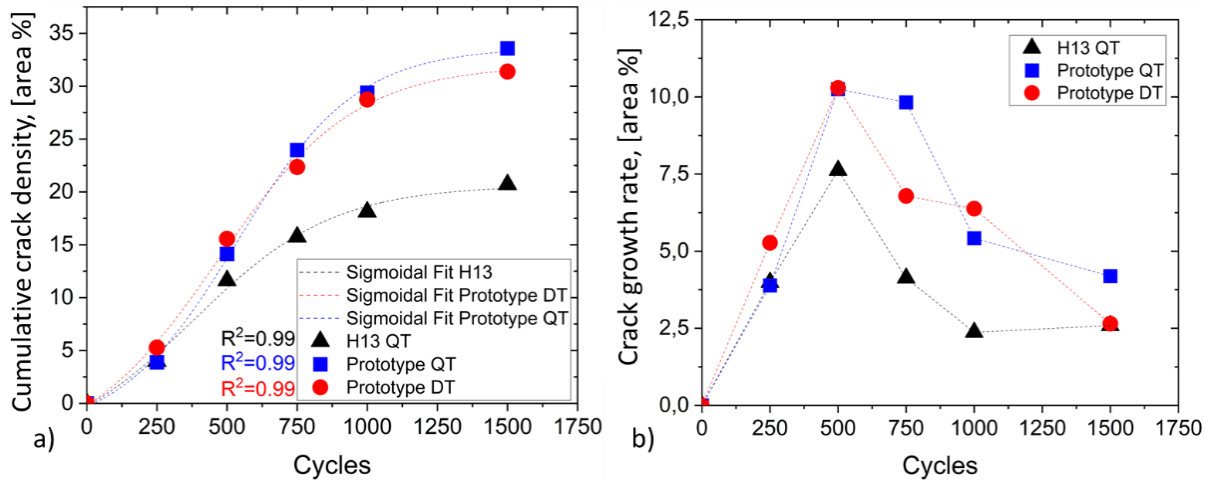


**Figure 15. a) heat-checking growth rate vs. TF cycles, and b) cumulative heat check density**

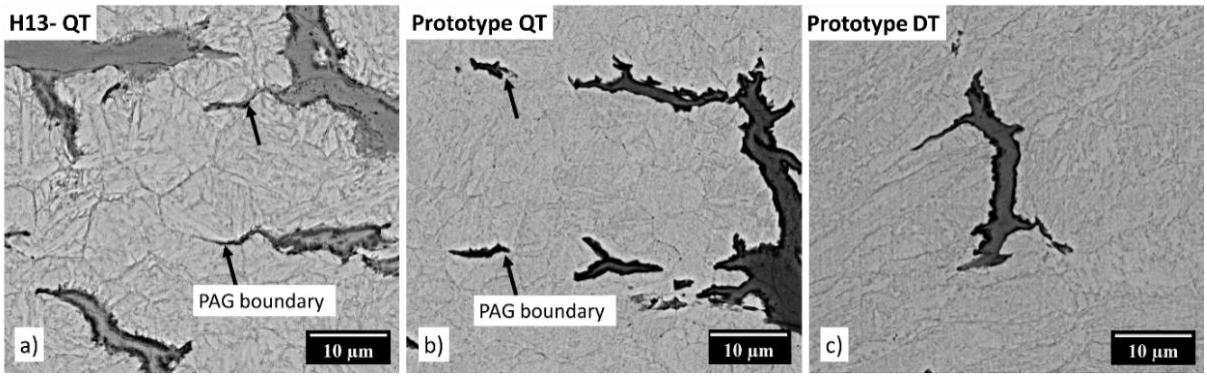


**Figure 16. Carefully polished, and chemically etched surfaces (Nital 2%), after 500 cycles of TF (630°C↔60°C), a) QT H13 (2×2h at 610°C, 440 HV1), b) QT prototype (2×2h at 610°C, 470 HV1) , and c) DT prototype (2×2h at 630°C, 480 HV1)**

### 3.4.2. Thermal Fatigue crack penetration

A cross sectional view of the subsurface crack penetration after completion of the tests at 1500 cycles is shown in Figure 16. In all samples, cracks are filled by oxides (Figs. 17a-c) a very typical phenomenon accompanying thermal fatigue damage in harsh environments (e.g., water cooling, air, and combustion gases). Crack filling by oxidation is enhanced due to larger free surface area within the cracks, and the oxide product, having a different CTE and specific molar volume compared to the metal matrix, introduces extra tensile stresses at the crack tip, leading to enhanced plastic yielding, and oxide induced crack propagation [25].

Fig. 17a clarifies that the maximum crack penetration depth is larger in H13 compared with the prototype steels (Figs. 17b, and c). Indeed, the maximum crack depth in H13 was ~115

µm, while in case of both QT and DT prototypes, this value was ~80 µm. The larger depth of the leading cracks in H13 might partially explain the less heat check density on its surface, as the thermal stresses seem to be accommodated by the propagation of the existing cracks, and the growth of the adjacent cracks, appearing noticeably short in Fig 16a, is retarded. The average crack depth was 44±32 µm, 57±18 µm, and 62±13 µm, for H13, QT prototype and DT prototype, respectively. These values were measured on 3 representative 100 x magnification, by adding the average oxide layer thickness to the length of the cracks as shown in Figs. 18a, and b.

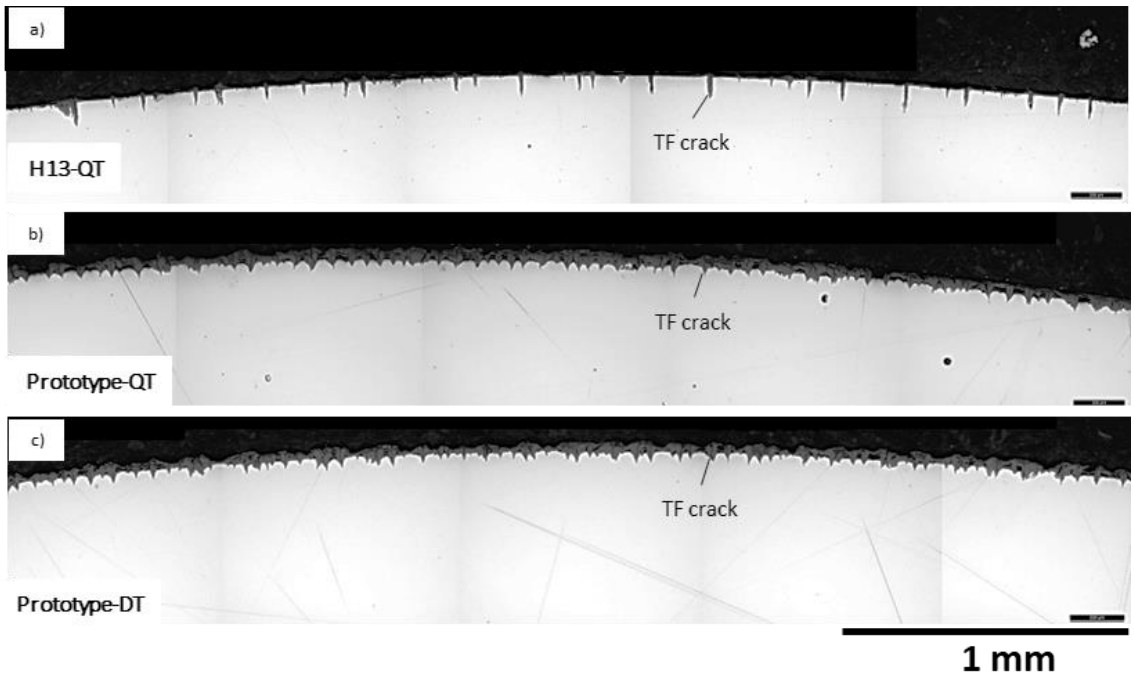


**Figure 17. cross-sectional view of crack propagation depths after 1500 cycles of TF (630°C↔60°C) : a) QT H13 (2×2h at 610°C, 440 HV1), b) QT prototype (2×2h at 610°C, 475 HV1) , and c) DT prototype (2×2h at 630°C, 480 HV1)**

In prototypes, the content of the elements Cr and Si was lower than that of H13 steel. The element Si can reduce the steam oxidation rates of Cr containing steels at temperatures above 650°C through the formation of $SiO_2$ protective films. Due to the lower Si-, and Cr-content, the oxidation product in modified grades seem to be larger in volume. The average surface oxide scale thickness in H13 was around 7±2 µm, while in both DT and QT prototypes this value was 25±5 and ~28±7 µm, respectively. In both cases the oxide scales were iron oxides rich in Cr, Mo, Si and Mn according to EDS analysis. The current results suggests that chemistry can be adjusted by ~ 3.0 wt.% Cr and up to 0.3 wt.% Si according to the suggestions of Norström [72]. However, this must be noted that the current experiments were carried out in air, and cooling medium was tapping water, therefore the current test condition can be considered exaggerated with respect to those in most common hot working applications like die-casting, hot-extrusion, and hot-forging. A summary of the measurements results is reported in table 5.

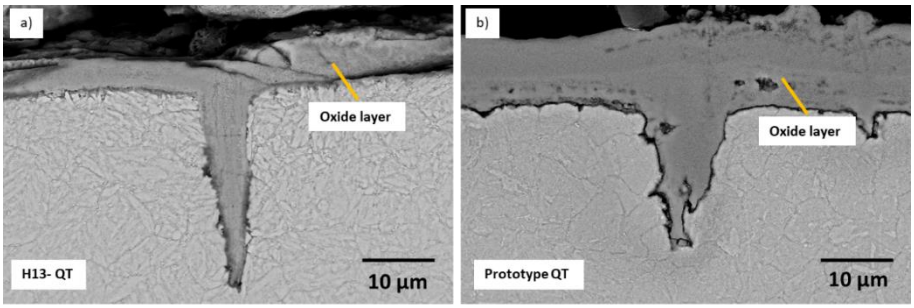


**Figure 18. Oxide layer thickness and TF crack filling by oxidation damage in a) QT H13, and b) QT prototype**

**Table 5. TF crack depth measurement results**

| | Maximum crack depth [µm] | Average crack depth [µm] | Penetrating crack density (/mm) | Average oxide thickness [µm] |
|---|---|---|---|---|
| H13 QT | 115 (108) | 44±32 (37) | 15 | 7±2 |
| Prototype QT | 83 (55) | 57±18 (29) | 17 | 28±7 |
| Prototype DT | 85 (60) | 62±13 (37) | 23 | 25±5 |

* **Numbers in parentheses refer to the length excluding the average oxide scale thickness**

### 3.4.3. Thermomechanical softening , and hot hardness at testing temperature

Thermomechanical softening after completion of the tests is plotted in Figure 19 . In H13, the minimum hardness (maximum softening) was ~375 HV1 at the surface (Fig.19a), roughly around 15% drop when normalized by the core hardness (Fig. 19b). In QT prototype the minimum hardness was ~425 HV1, manifesting a 10% drop vs. the core hardness, while in DT prototype, initially tempered at a higher temperature (i.e., 630ºC vs. 610ºC for both H13 and QT prototype), only a 7.5% drop in hardness was recorded (Figs.19a, and b). It is evident that the hardness drop in the new prototype steel is lower than that of H13, which agrees with the tempering resistance results. Moreover, the hardness recovery slope is higher in prototype alloys compared with that of H13. In H13, the softening depth was almost 2.5 mm while in prototypes it was slightly smaller (i.e., 2 mm).

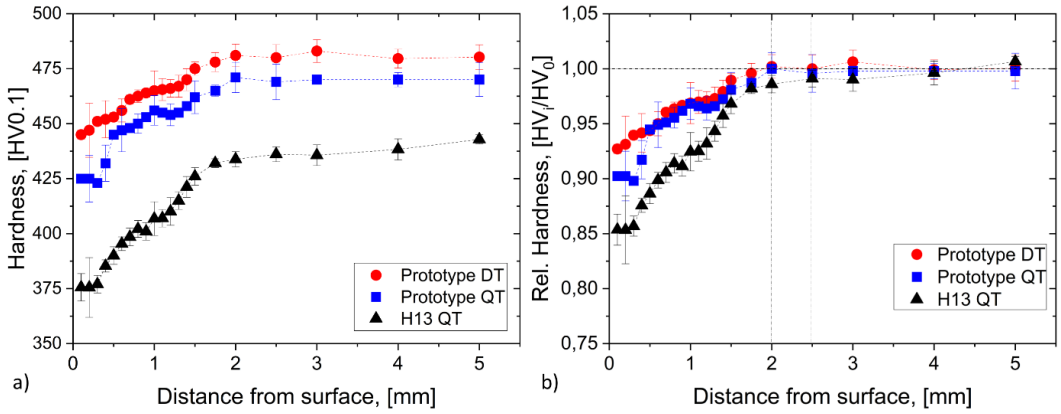


**Figure 19. Thermomechanical softening profile after 1500 cycles of TF (630°C↔60°C): a) measured microhardness, b) microhardness normalized by core hardness (i.e., $HV_i$ / $HV_0$)**

The hot hardness manifests another significant result at 630°C (i.e., TF test temperature). The hot hardness results (Table 6) confirm a higher hot strength for prototype alloys compared with steel H13, where the DT and QT prototype show 428±11 and 435±15 HV10, respectively. At the same time, steel H13 undergoes a significant softening and shows a hardness of 318±33. This result further emphasizes the importance of thermally stable secondary carbides in the microstructure of prototype alloys, even with lower C contents than H13 steel. Moreover, the complementary effect of enhanced thermal conductivity should be considered.

**Table 6. Hot hardness results**

| Sample | Hot hardness at 630°C, [HV10] |
|---|---|
| H13 QT | 318±33 |
| Prototype QT | 435±15 |
| Prototype DT | 428±11 |

### 3.4.4. Thermal Fatigue damage discussion

The cumulative heat check evolution on the surface by the initial 500 cycles showed that the heat check density was somehow similar for H13 and the prototype alloys (see Fig. 15a). At 750 cycles onwards, the heat check density growth rate seemed to slow down faster in H13 (Fig. 15), probably because of larger oxidation resistance, as well as larger penetration depth of the leading cracks to the core. This was backed by the observation of crack penetration depth after the completion of the tests, suggesting that in H13 steel, leading cracks grow deeper into the core as shown in Fig. 17. By considering the improved thermal conductivity, hot hardness, thermal, and thermomechanical softening resistance of the prototype tool steel, the crack penetration depth seems to correlate to the gradual softening of the tool steel. This might be reasonable, as the crack growth is accelerated by the local plastic yielding of the tool material ahead of the crack, therefore, the higher the hardness, the larger the local yield strength. Indeed, the hot hardness of DT and QT prototype alloys at 630°C (i.e., 428, and 435 HV10, respectively) was significantly larger than that of H13 (i.e., 318 HV10). This practically means that the inferior hot hardness of H13 compared to the prototype led to easier crack propagation towards the core in the former. Moreover, the larger thermal conductivity of the prototype alloys should have reduced the thermal gradients during the cyclic heating and cooling. The higher thermal conductivity of the prototype alloys was a direct consequence of a lower Si- and Cr-content. On the other hand, lowering the amount of the elements Cr and Si caused a greater oxidation damage in prototypes considering the TF test condition in this work.

About 80% of the dies in HPDC fail by crack initiation and penetration into the core by heat checking [8]. Likely, the main reason for the increased thermal fatigue resistance in prototype alloys, in view of the crack penetration depth is their increased tempering resistance, and hot strength. Especially in case of test or service temperatures above the die tempering temperature, tempering resistance becomes the most significant factor [73]. Of course, it is also necessary for the tool material to possess low CTE, high thermal conductivity, maintain high hot yield strength, in combination with acceptable toughness [74–76]. The tool maintenance during the die casting service comprises lubrication after each casting and

periodic cleaning by shot blasting [25]. In view of results obtained in this work, this mechanical polishing might be helpful in the elimination of the shallower heat checks observed in prototype alloys, and also any surface oxidation, thus increasing the durability of the die, while it cannot be as effective in case of deeper cracks in H13. On the other hand, it appears that a more frequent maintenance might be needed to avoid severe surface defects on the cast parts due to the dense heat check network, in view of the larger oxidation damage in prototype alloys. This is plausible for all processes involving severe oxidation (e.g., hot forging), while it is much less important for processes where oxidation is just a minor form of damage (e.g., die casting, hot extrusion). Therefore, in case the L-PBF processability and achievable tempered hardness by a leaner C prototype alloy is not compromised significantly, slight increase in Cr content (~3 wt.%) might result in a better oxidation resistance.

### 3.5. Proof of concept

An injection molding die was processed on an industrial Renishaw 500 Q-flex machine with the dimensions of 150 mm x 110 mm x 30 mm using 170°C plate preheating (Fig. 20a). The stress concentrators at the edges of near surface conformal cooling channels were printed successfully without any apparent cracking before and after sand blasting and edge blunting (Figs. 20 b, and c).

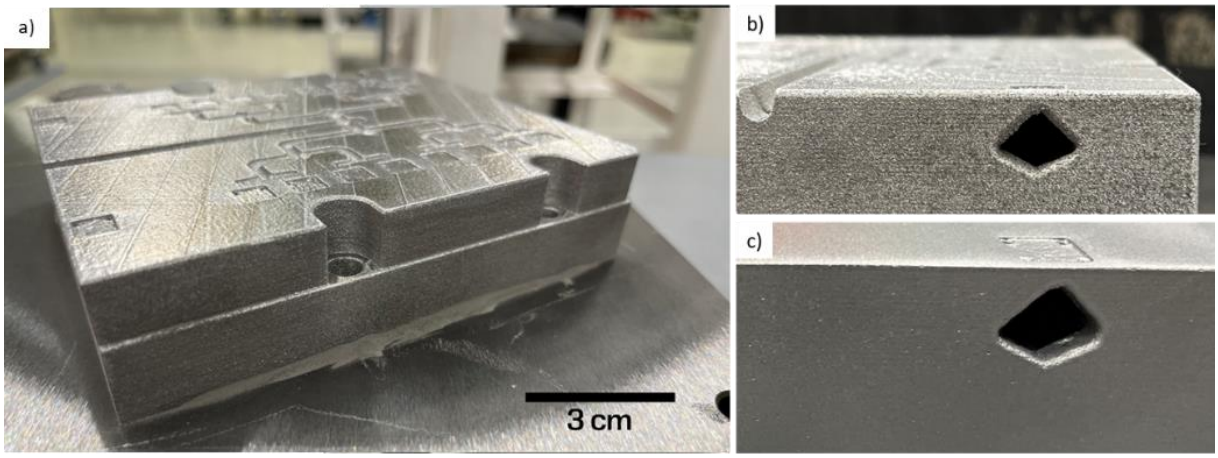


**Figure 20. A demo mold in prototype alloy, a) general view, b) sharp angle cooling channels before shot blasting, and c) after shot blasting**

The tensile and impact properties in AB condition, and at two commonly used hardness levels of 540 HV1 (51.5 HRC) and 450 HV1 (45 HRC) after direct double tempering (DT) at 605°C, and 650°C respectively are reported in Table 7. In AB condition and at a hardness level of 485 HV1, a yield strength of 1530 MPa and a tensile strength of 1607 MPa was recorded. The elongation and area reduction were 17% and 57% respectively. At a hardness of 540 HV10 (51.5 HRC), a yield strength of 1730 MPa, tensile strength of 1833 MPa and elongation of 11.8% and area reduction of 63% was recorded. These values were 1413 MPa, 1520 MPa, 12.3% and 61% for the samples tempered to 450 HV10. The impact toughness at 450 HV10 was 22.3±0.9 J, while at 540 HV10 hardness level an average impact toughness of 10.3±2.3 was recorded. The stress-strain curves are shown in Fig. 21, and SEM micrographs on the fracture surfaces can be found in supplementary file 3.

**Table 7. Tensile and impact properties in as built state as well as directly tempered condition at two hardness levels of 51, and 45 HRC**

| Tempering temperature [°C] 2x2h | Hardness [HV1] | Hardness [HRC] | CVN Impact toughness [J] | Yield Strength [MPa] | Tensile strength [MPa] | Elongation (%) | Area reduction (%) |
|---|---|---|---|---|---|---|---|
| AB | 485±15 | - | 33.6±0.8 | 1530±30 | 1607±6 | 17.0±0.9 | 57±1 |
| 605°C | 540±9 | 51.5 | 10.3±2.3 | 1730±20 | 1833±6 | 11.8±0.3 | 63±1 |
| 650°C | 450±3 | 45.0 | 22.3±0.9 | 1413±6 | 1520±1 | 12.3±0.3 | 61±2 |

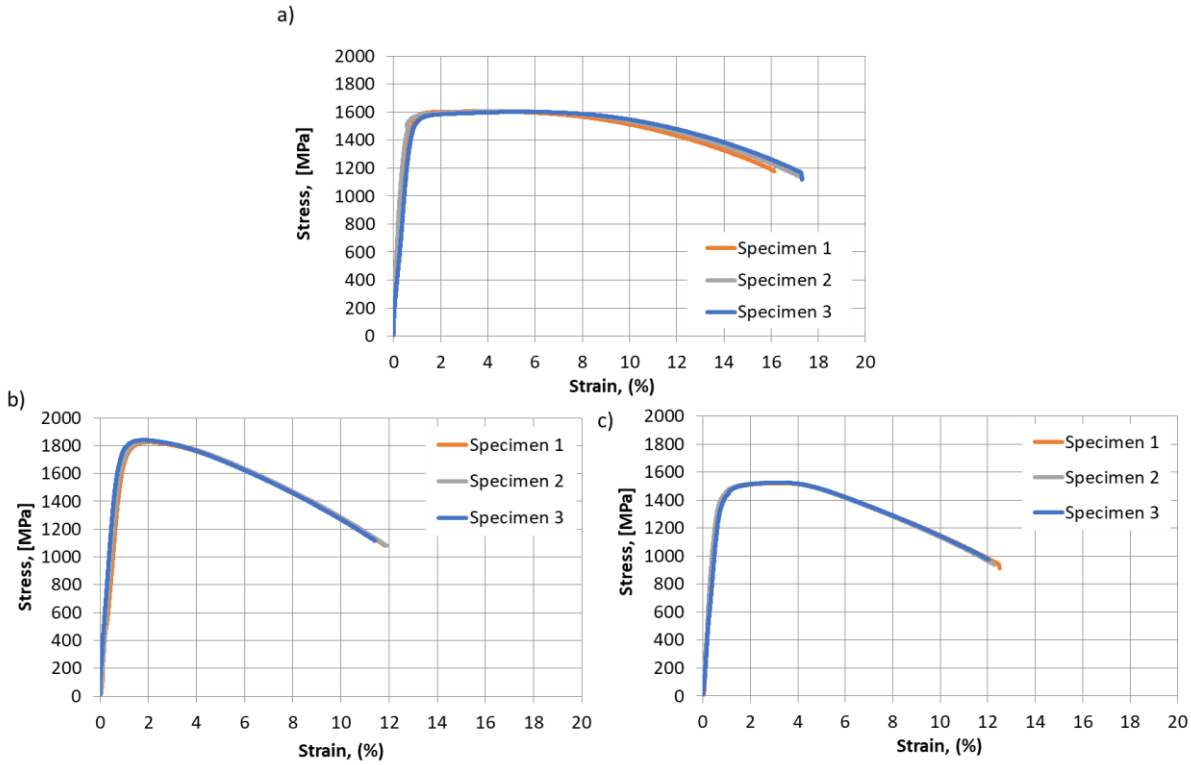


**Figure 21. Engineering stress-strain curves of tensile testing of prototype alloy in , a) AB condition, b) Directly tempered at 605°C (51.5 HRC), and c) directly tempered at 650°C (45 HRC)**

The tensile strength values, and impact toughness at these two hardness levels are in line with the steel H13 in wrought, quenched and tempered condition according to literature [77,78]. At a hardness level of 450 HV10 (~45 HRC), Charpy-V impact toughness of 22 J at room temperature is higher than the requirements given in NADCA#207-2003 specifying a minimum of 11 J, and 14 J for premium and superior quality hot work tool steel, respectively [78].

## 4. Conclusions

In this work an experimental hot work tool steel with lower carbon (~0.25 wt.%) content compared with those of medium carbon counterparts (~ 0.4 wt.%) was processed by L-PBF

and characterized in view of microstructure, tempering behavior and thermal fatigue resistance. The following conclusions were made.

- The processability was enhanced due to lower dilatation during martensitic transformation (~18 %), lower as-built hardness (485 HV1 vs. ~600 HV1), and significantly higher Charpy V notch impact toughness (i.e., > 30 J). This was further improved by a reduced residual stress state compared to literature values.
- Thermal conductivity was improved because of reduction of the elements Si and C and the formation of tempering carbides at elevated temperatures.
- Tempering resistance and hot hardness were improved compared with H13 steel, due to larger Mo to Cr ratio, and lower Si, leading to a shift of secondary hardness peaks to higher temperatures, and more sluggish coarsening of the Mo, and V rich secondary carbides.
- In quenched and tempered prototype, reduced driving force for the precipitation of coarse V rich carbides ($V_8C_7$) and carbonitrides ($V_2(C,N)$) during austenitization, resulted in a larger supersaturation of quenched martensite in elements V, and C. This leads to a strong fine *secondary* carbides precipitation during tempering, contributing significantly to the enhanced tempering resistance over H13.
- Compared with H13, thermal fatigue damage (heat checking) was more severe on the surface of prototypes due to a finer prior austenite grain size (larger grain boundary area) and lower Cr, leading to more oxidation attacks at the grain boundaries.
- Compared with H13, Thermal Fatigue crack depth was significantly lower in prototypes because of improved thermal conductivity, thermomechanical softening resistance, and significantly improved hot hardness.
- A proof of concept was demonstrated to be successfully processed using the new chemistry and mechanical properties after direct double tempering to two common tempered hardness levels of 45, and 51 HRC was in line with wrought H13 steel.

**Acknowledgement**

We thank the Center for Synchrotron Radiation at the TU Dortmund on beamline 9 for carrying out the diffraction experiments. Especially, we thank Dr. Christian Sternemann of TU

Dortmund (Maria-Goeppert-Mayer-Str. 2, 44221 Dortmund, Germany) for his support during the diffraction experiments.

## References

[1] N. Haghdadi, M. Laleh, M. Moyle, S. Primig, Additive manufacturing of steels: a review of achievements and challenges, J. Mater. Sci. 56 (2021) 64–107. https://doi.org/10.1007/s10853-020-05109-0.

[2] P. Bajaj, A. Hariharan, A. Kini, P. Kürnsteiner, D. Raabe, E.A. Jägle, Steels in additive manufacturing: A review of their microstructure and properties, Mater. Sci. Eng. A 772 (2020) 138633. https://doi.org/10.1016/j.msea.2019.138633.

[3] K. Li, T. Yang, N. Gong, J. Wu, X. Wu, D.Z. Zhang, L.E. Murr, Additive manufacturing of ultra-high strength steels: A review, J. Alloys Compd. 965 (2023) 171390. https://doi.org/10.1016/j.jallcom.2023.171390.

[4] M. Moshiri, D. Loaldi, F. Zanini, D. Sgaravato, S. Carmignato, G. Tosello, Analysis of an as-built metal additively manufactured tool cavity insert performance and advantages for plastic injection moulding, J. Manuf. Process. 61 (2021) 369–382. https://doi.org/10.1016/j.jmapro.2020.11.035.

[5] M. Moshiri, M. Raza, M. Sahlab, A.A. Malik, A. Bilberg, G. Tosello, Value Chain Comparison of Additively and Conventionally Manufactured Multi-Cavity Tool Steel Inserts: An Injection Molding Industrial Case Study for High-Volume Production, Appl. Sci. 12 (2022). https://doi.org/10.3390/app122010410.

[6] N. Asnafi, Application of Laser-Based Powder Bed Fusion for Direct Metal Tooling, Metals 11 (2021). https://doi.org/10.3390/met11030458.

[7] D. Klobčar, J. Tušek, B. Taljat, Thermal fatigue of materials for die-casting tooling, Mater. Sci. Eng. A 472 (2008) 198–207. https://doi.org/10.1016/j.msea.2007.03.025.

[8] J. Sjöström, J. Bergström, Thermal fatigue testing of chromium martensitic hot-work tool steel after different austenitizing treatments, Proc. Int. Conf. Adv. Mater. Process. Technol. 153–154 (2004) 1089–1096. https://doi.org/10.1016/j.jmatprotec.2004.04.158.

[9] Y. He, M. Zhong, J. Beuth, B. Webler, A study of microstructure and cracking behavior of H13 tool steel produced by laser powder bed fusion using single-tracks, multi-track pads, and 3D cubes, J. Mater. Process. Technol. 286 (2020) 116802. https://doi.org/10.1016/j.jmatprotec.2020.116802.

[10] H.-H. König, N.H. Pettersson, A. Durga, S. Van Petegem, D. Grolimund, A.C. Chuang, Q. Guo, L. Chen, C. Oikonomou, F. Zhang, G. Lindwall, Solidification modes during additive manufacturing of steel revealed by high-speed X-ray diffraction, Acta Mater. 246 (2023) 118713. https://doi.org/10.1016/j.actamat.2023.118713.

[11] E.B. Fonseca, J.D. Escobar, A.H.G. Gabriel, G.G. Ribamar, T. Boll, É.S.N. Lopes, Tempering of an additively manufactured microsegregated hot-work tool steel: A high-temperature synchrotron X-ray diffraction study, Addit. Manuf. 55 (2022) 102812. https://doi.org/10.1016/j.addma.2022.102812.

[12] A. Röttger, J. Boes, F. Großwendt, S. Weber, Description of a new concept for the development of adapted hot-work tool steels for laser-powder bed fusion, Addit. Manuf. 61 (2023) 103292. https://doi.org/10.1016/j.addma.2022.103292.

[13] R. Mertens, B. Vrancken, N. Holmstock, Y. Kinds, J.-P. Kruth, J. Van Humbeeck, Influence of Powder Bed Preheating on Microstructure and Mechanical Properties of H13 Tool Steel SLM Parts, Laser Assist. Net Shape Eng. 9 Int. Conf. Photonic Technol. Proc. LANE 2016 Sept. 19-22 2016 Fürth Ger. 83 (2016) 882–890. https://doi.org/10.1016/j.phpro.2016.08.092.

[14] F. Deirmina, P.A. Davies, N. Dixit, R. Siriki, M. Pellizzari, Production and Characterization of a Modified Hot Work Tool Steel by Laser Powder Bed Fusion, Metall. Mater. Trans. A 53 (2022) 2642–2651. https://doi.org/10.1007/s11661-022-06694-2.
[15] J. Platl, H. Leitner, C. Turk, A.G. Demir, B. Previtali, R. Schnitzer, Defects in a Laser Powder Bed Fused Tool Steel, Adv. Eng. Mater. 23 (2021) 2000833. https://doi.org/10.1002/adem.202000833.
[16] L. Wu, S. Das, W. Gridin, S. Leuders, M. Kahlert, M. Vollmer, T. Niendorf, Hot Work Tool Steel Processed by Laser Powder Bed Fusion: A Review on Most Relevant Influencing Factors, Adv. Eng. Mater. 23 (2021) 2100049. https://doi.org/10.1002/adem.202100049.
[17] N. Wilda, J. Giedenbacher, A. Huskic, Material properties of AISI H10 (32CrMoV12-28) hot work tool steel processed by Laser Powder Bed Fusion with 200°C substrate preheating temperature, 4th Int. Conf. Ind. 40 Smart Manuf. 217 (2023) 1008–1017. https://doi.org/10.1016/j.procs.2022.12.299.
[18] A. Vogelpoth, J. Saewe, H.-G. Krull, S. Richert, P. Weiland, T. Nerzak, F. Eibl, F. Pastors, Additive Manufacturing of Tool Steels, Steel Res. Int. 94 (2023) 2200372. https://doi.org/10.1002/srin.202200372.
[19] F. Pixner, R. Buzolin, F. Warchomicka, M. Dománková, M. Čaplovičová, F. Riedlsperger, S. Fritsche, M. Orłowska, J. Domitner, M. Lasnik, N. Enzinger, Influence of process and heat input on the microstructure and mechanical properties in wire arc additive manufacturing of hot work tool steels, Mater. Sci. Eng. A 888 (2023) 145799. https://doi.org/10.1016/j.msea.2023.145799.
[20] M. Yuan, Y. Cao, S. Karamchedu, S. Hosseini, Y. Yao, J. Berglund, L. Liu, L. Nyborg, Characteristics of a modified H13 hot-work tool steel fabricated by means of laser beam powder bed fusion, Mater. Sci. Eng. A 831 (2022) 142322. https://doi.org/10.1016/j.msea.2021.142322.
[21] H. Berns, F. Wendl, Effect of carbon content in CrMoV hot working tool steel, Steel Res. 57 (1986) 671–676. https://doi.org/10.1002/srin.198600848.
[22] G. Roberts, G. Krauss, R. Kennedy, Tool Steels, ASM International, 1998. https://doi.org/10.31399/asm.tb.ts5.9781627083584.
[23] D. Delagnes, P. Lamesle, M.H. Mathon, N. Mebarki, C. Levaillant, Influence of silicon content on the precipitation of secondary carbides and fatigue properties of a 5%Cr tempered martensitic steel, Mater. Sci. Eng. A 394 (2005) 435–444. https://doi.org/10.1016/j.msea.2004.11.050.
[24] M. Åsberg, G. Fredriksson, S. Hatami, W. Fredriksson, P. Krakhmalev, Influence of post treatment on microstructure, porosity and mechanical properties of additive manufactured H13 tool steel, Mater. Sci. Eng. A 742 (2019) 584–589. https://doi.org/10.1016/j.msea.2018.08.046.
[25] A. Persson, S. Hogmark, J. Bergström, Failure modes in field-tested brass die casting dies, J. Mater. Process. Technol. 148 (2004) 108–118. https://doi.org/10.1016/j.jmatprotec.2004.01.052.
[26] A. Röttger, J. Boes, W. Theisen, M. Thiele, C. Esen, A. Edelmann, R. Hellmann, Microstructure and mechanical properties of 316L austenitic stainless steel processed by different SLM devices, Int. J. Adv. Manuf. Technol. 108 (2020) 769–783. https://doi.org/10.1007/s00170-020-05371-1.
[27] P.J. Konijnenberg, S. Zaefferer, D. Raabe, Assessment of geometrically necessary dislocation levels derived by 3D EBSD, Acta Mater. 99 (2015) 402–414. https://doi.org/10.1016/j.actamat.2015.06.051.
[28] L. Lutterotti, Maud: a Rietveld analysis program designed for the internet and experiment integration, Acta Crystallogr A 56 (2000) 54.
[29] C.E.S. Bernardes, A. Joseph, M.E.M. da Piedade, Some practical aspects of heat capacity determination by differential scanning calorimetry, Thermochim. Acta 687 (2020) 178574. https://doi.org/10.1016/j.tca.2020.178574.
[30] J. Krell, A. Röttger, U. Ziesing, W. Theisen, Influence of precipitation hardening on the high-temperature sliding wear resistance of an aluminium alloyed iron-nickel base alloy, Tribol. Int. 148 (2020) 106342. https://doi.org/10.1016/j.triboint.2020.106342.

[31] M. Duan, G. Bai, S. Guo, Y. Peng, X. Liu, W. Zhang, X. Zhang, Y. Huang, J. Liu, G. Gao, J. Kong, Q. Zhou, K. Wang, Dynamic tensile mechanical properties of 18Ni350 maraging steel fabricated by wire arc additive manufacturing, J. Mater. Res. Technol. 25 (2023) 5426–5442. https://doi.org/10.1016/j.jmrt.2023.06.276.
[32] E.A. Jägle, Z. Sheng, P. Kürnsteiner, S. Ocylok, A. Weisheit, D. Raabe, Comparison of Maraging Steel Micro- and Nanostructure Produced Conventionally and by Laser Additive Manufacturing, Materials 10 (2017). https://doi.org/10.3390/ma10010008.
[33] C.-Y. Chou, N.H. Pettersson, A. Durga, F. Zhang, C. Oikonomou, A. Borgenstam, J. Odqvist, G. Lindwall, Influence of solidification structure on austenite to martensite transformation in additively manufactured hot-work tool steels, Acta Mater. 215 (2021) 117044. https://doi.org/10.1016/j.actamat.2021.117044.
[34] F. Deirmina, N. Peghini, B. AlMangour, D. Grzesiak, M. Pellizzari, Heat treatment and properties of a hot work tool steel fabricated by additive manufacturing, Mater. Sci. Eng. A 753 (2019) 109–121. https://doi.org/10.1016/j.msea.2019.03.027.
[35] W. Hearn, K. Lindgren, J. Persson, E. Hryha, In situ tempering of martensite during laser powder bed fusion of Fe-0.45C steel, Materialia 23 (2022) 101459. https://doi.org/10.1016/j.mtla.2022.101459.
[36] G. Carasi, B. Yu, E. Hutten, H. Zurob, R. Casati, M. Vedani, Effect of Heat Treatment on Microstructure Evolution of X38CrMoV5-1 Hot-Work Tool Steel Produced by L-PBF, Metall. Mater. Trans. A 52 (2021) 2564–2575. https://doi.org/10.1007/s11661-021-06248-y.
[37] S. Amirabdollahian, F. Deirmina, L. Harris, R. Siriki, M. Pellizzari, P. Bosetti, A. Molinari, Towards controlling intrinsic heat treatment of maraging steel during laser directed energy deposition, Scr. Mater. 201 (2021) 113973. https://doi.org/10.1016/j.scriptamat.2021.113973.
[38] H. Ding, T. Liu, J. Wei, L. Chen, F. Cao, B. Zhang, R. Luo, X. Cheng, Microstructure and tempering softening mechanism of modified H13 steel with the addition of Tungsten, Molybdenum, and lowering of Chromium, Mater. Des. 224 (2022) 111317. https://doi.org/10.1016/j.matdes.2022.111317.
[39] B. Hutchinson, J. Hagström, O. Karlsson, D. Lindell, M. Tornberg, F. Lindberg, M. Thuvander, Microstructures and hardness of as-quenched martensites (0.1–0.5%C), Acta Mater. 59 (2011) 5845–5858. https://doi.org/10.1016/j.actamat.2011.05.061.
[40] H. Bhadeshia, R. Honeycombe, Chapter 5 - Formation of Martensite, in: H. Bhadeshia, R. Honeycombe (Eds.), Steels Microstruct. Prop. Fourth Ed., Butterworth-Heinemann, 2017: pp. 135–177. https://doi.org/10.1016/B978-0-08-100270-4.00005-6.
[41] G. Krauss, Martensite in steel: strength and structure, Mater. Sci. Eng. A 273–275 (1999) 40–57. https://doi.org/10.1016/S0921-5093(99)00288-9.
[42] S. Ramesh Babu, T.P. Davis, T. Haas, A. Jarvenpää, J. Kömi, D. Porter, Image Processing Tool Quantifying Auto-Tempered Carbides in As-Quenched Low Carbon Martensitic Steels, Metals 10 (2020). https://doi.org/10.3390/met10020171.
[43] S. Amirabdollahian, F. Deirmina, M. Pellizzari, P. Bosetti, A. Molinari, Tempering behavior of a direct laser deposited hot work tool steel: Influence of quenching on secondary hardening and microstructure, Mater. Sci. Eng. A 814 (2021) 141126. https://doi.org/10.1016/j.msea.2021.141126.
[44] J. Kunz, S. Herzog, A. Kaletsch, C. Broeckmann, Influence of initial defect density on mechanical properties of AISI H13 hot-work tool steel produced by laser powder bed fusion and hot isostatic pressing, Powder Metall. 65 (2022) 1–12. https://doi.org/10.1080/00325899.2021.1934634.
[45] M. Ackermann, J. Šafka, L. Voleský, J. Bobek, J.R. Kondapally, Impact Testing of H13 Tool Steel Processed with Use of Selective Laser Melting Technology, Mater. Sci. Forum 919 (2018) 43–51. https://doi.org/10.4028/www.scientific.net/MSF.919.43.
[46] M. Narvan, A. Ghasemi, E. Fereiduni, S. Kendrish, M. Elbestawi, Part deflection and residual stresses in laser powder bed fusion of H13 tool steel, Mater. Des. 204 (2021) 109659. https://doi.org/10.1016/j.matdes.2021.109659.

[47] J.J. Yan, D.L. Zheng, H.X. Li, X. Jia, J.F. Sun, Y.L. Li, M. Qian, M. Yan, Selective laser melting of H13: microstructure and residual stress, J. Mater. Sci. 52 (2017) 12476–12485. https://doi.org/10.1007/s10853-017-1380-3.
[48] F. Deirmina, P.A. Davies, R. Casati, Effects of Powder Atomization Route and Post-Processing Thermal Treatments on the Mechanical Properties and Fatigue Resistance of Additively Manufactured 18Ni300 Maraging Steel, Adv. Eng. Mater. (2021) 2101011.
[49] L. Cheng, C.M. Brakman, B.M. Korevaar, E.J. Mittemeijer, The tempering of iron- carbon martensite; dilatometric and calorimetric analysis, Metall. Trans. A 19 (1988) 2415–2426. https://doi.org/10.1007/BF02645469.
[50] M. Hunkel, J. Dong, J. Epp, D. Kaiser, S. Dietrich, V. Schulze, A. Rajaei, B. Hallstedt, C. Broeckmann, Comparative Study of the Tempering Behavior of Different Martensitic Steels by Means of In-Situ Diffractometry and Dilatometry, Materials 13 (2020). https://doi.org/10.3390/ma13225058.
[51] R.E. Reed-Hill, R. Abbaschian, R. Abbaschian, Physical metallurgy principles, Van Nostrand New York, 1973.
[52] K.S. Cho, H. Kwon, Effect of Si addition on secondary hardening of alloy steels, Met. Mater. Int. 23 (2017) 632–638. https://doi.org/10.1007/s12540-017-7162-2.
[53] R.A. Mesquita, H.-J. Kestenbach, Complete model for effects of silicon in 5%Cr hot work tool steels, Int. Heat Treat. Surf. Eng. 4 (2010) 145–151. https://doi.org/10.1179/174951410X12851626812899.
[54] E. Kozeschnik, H.K.D.H. Bhadeshia, Influence of silicon on cementite precipitation in steels, Mater. Sci. Technol. 24 (2008) 343–347. https://doi.org/10.1179/174328408X275973.
[55] G. Miyamoto, J.C. Oh, K. Hono, T. Furuhara, T. Maki, Effect of partitioning of Mn and Si on the growth kinetics of cementite in tempered Fe–0.6 mass% C martensite, Acta Mater. 55 (2007) 5027–5038. https://doi.org/10.1016/j.actamat.2007.05.023.
[56] M. Preciado, M. Pellizzari, Influence of deep cryogenic treatment on the thermal decomposition of Fe–C martensite, J. Mater. Sci. 49 (2014) 8183–8191. https://doi.org/10.1007/s10853-014-8527-2.
[57] J. Krell, A. Röttger, K. Geenen, W. Theisen, General investigations on processing tool steel X40CrMoV5-1 with selective laser melting, J. Mater. Process. Technol. 255 (2018) 679–688. https://doi.org/10.1016/j.jmatprotec.2018.01.012.
[58] B. Sonderegger, E. Kozeschnik, H. Leitner, H. Clemens, J. Svoboda, F.D. Fischer, P. Staron, Kinetics of Precipitation in a Complex Hot-work Tool Steel, Steel Res. Int. 81 (2010) 64–73. https://doi.org/10.1002/srin.200900069.
[59] A. Eser, C. Broeckmann, C. Simsir, Multiscale modeling of tempering of AISI H13 hot-work tool steel – Part 1: Prediction of microstructure evolution and coupling with mechanical properties, Comput. Mater. Sci. 113 (2016) 280–291. https://doi.org/10.1016/j.commatsci.2015.11.020.
[60] S. Morito, H. Tanaka, R. Konishi, T. Furuhara, T. Maki, The morphology and crystallography of lath martensite in Fe-C alloys, Acta Mater. 51 (2003) 1789–1799. https://doi.org/10.1016/S1359-6454(02)00577-3.
[61] S. Morito, H. Yoshida, T. Maki, X. Huang, Effect of block size on the strength of lath martensite in low carbon steels, Proc. Int. Conf. Martensitic Transform. 438–440 (2006) 237–240. https://doi.org/10.1016/j.msea.2005.12.048.
[62] N. Mebarki, D. Delagnes, P. Lamesle, F. Delmas, C. Levaillant, Relationship between microstructure and mechanical properties of a 5% Cr tempered martensitic tool steel, 13th Int. Conf. Strength Mater. 387–389 (2004) 171–175. https://doi.org/10.1016/j.msea.2004.02.073.
[63] A.S. Kurlov, A.I. Gusev, Effect of nonstoichiometry on the lattice constant of cubic vanadium carbide VCy, Phys. Solid State 59 (2017) 1520–1525. https://doi.org/10.1134/S1063783417080133.
[64] L. Chen, Z. Jiang, First-principles study on a new type of quaternary carbonitride VWCN with outstanding mechanical properties, Int. J. Refract. Met. Hard Mater. 92 (2020) 105319. https://doi.org/10.1016/j.ijrmhm.2020.105319.

[65] Z. Lv, S. Xiao, Z. Xiao, L. Qian, W. Wang, Y. Zhou, W. Fu, Structural properties and bonding characteristic of interfaces between VN and VC from density functional calculations, J. Alloys Compd. 718 (2017) 139–149. https://doi.org/10.1016/j.jallcom.2017.04.325.
[66] A. Shibata, T. Nagoshi, M. Sone, S. Morito, Y. Higo, Evaluation of the block boundary and sub-block boundary strengths of ferrous lath martensite using a micro-bending test, Mater. Sci. Eng. A 527 (2010) 7538–7544. https://doi.org/10.1016/j.msea.2010.08.026.
[67] F. Deirmina, M. Pellizzari, Strengthening mechanisms in an ultrafine grained powder metallurgical hot work tool steel produced by high energy mechanical milling and spark plasma sintering, Mater. Sci. Eng. A 743 (2019) 349–360. https://doi.org/10.1016/j.msea.2018.11.093.
[68] E.I. Galindo-Nava, P.E.J. Rivera-Díaz-del-Castillo, A model for the microstructure behaviour and strength evolution in lath martensite, Acta Mater. 98 (2015) 81–93. https://doi.org/10.1016/j.actamat.2015.07.018.
[69] K. Fuchs, HOT-WORK TOOL STEELS WITH IMPROVED PROPERTIES FOR DIE CASTING APPLICATIONS, in: 2006. https://api.semanticscholar.org/CorpusID:224497141.
[70] J. Wilzer, J. Küpferle, S. Weber, W. Theisen, Influence of Alloying Elements, Heat Treatment, and Temperature on the Thermal Conductivity of Heat Treatable Steels, Steel Res. Int. 86 (2015) 1234–1241. https://doi.org/10.1002/srin.201400294.
[71] Y. Sun, J. Wang, M. Li, Y. Wang, C. Li, T. Dai, M. Hao, H. Ding, Thermal and mechanical properties of selective laser melted and heat treated H13 hot work tool steel, Mater. Des. 224 (2022) 111295. https://doi.org/10.1016/j.matdes.2022.111295.
[72] L.-Å. Norström, M. Svensson, N. Öhrberg, Thermal-fatigue behaviour of hot-work tool steels, Met. Technol. 8 (1981) 376–381. https://doi.org/10.1179/030716981803275947.
[73] J. Sjöström, J. Bergström, Evaluation of the cyclic behaviour during high temperature fatigue of hot work tool steels, in: 2002: pp. 603–615.
[74] V. Ahuja, M. Jahedi, Heat checking-a comparison of five hot work tool steels for use in high pressure die casting dies, (2001).
[75] J.R. Davis, ASM specialty handbook: tool materials, ASM international, 1995.
[76] P. Roche, M. Beaton, B. Klarenfjord, O. Sandberg, Toughness and ductility--your die needs both, Giess.-PraxisGermany 10 (1998) 405–414.
[77] V. Leskovšek, Correlation between the KIc, the HRc and the Charpy V-Notch Test Results for H11/H13 Hot-work Tool Steels at Room Temperature, Steel Res. Int. 79 (2008) 306–313. https://doi.org/10.1002/srin.200806355.
[78] P. Hansson, Modern Prehardened Tool Steels in Die-Casting Applications, Mater. Manuf. Process. 24 (2009) 824–827. https://doi.org/10.1080/10426910902841753.